Supporting Information for "Probing Interfacial Effects on Ionization Energies: The Surprising Banality of Anion–Water Hydrogen Bonding at the Air/Water Interface"

Suranjan K. Paul and John M. Herbert*
Department of Chemistry and Biochemistry
The Ohio State University, Columbus, Ohio 43210 USA

June 15, 2021

Contents

*herbert@chemistry.ohio-state.edu

S1 Molecular Dynamics Simulations

S1.1 Force Field Parameters

We use the AMOEBA polarizable force field for water[1] and for all of the ions studied in this work. AMOEBA parameters for halide ions[2] and for sulfate[3] are available in the literature. Parameters for the remaining ions (and for SO_4^{2-}, as a consistency check) were obtained using a protocol developed by Ponder and co-workers,[4] which our group employed previously.[5] Initial values for the atom-centered multipoles were obtained using generalized distributed multipole analysis,[6] as implemented in the Psi4 program.[7] Geometries were optimized at the ωB97X-D/6-311+G* level and then the electrostatic potential was computed on a Cartesian grid at the ωB97X-D/aug-cc-pVTZ level. Final multipoles were computed by adjusting the initial values in order to fit to the electrostatic potential on the grid. Valence parameters including force constants for bond stretching and angle bending, along with van der Waals parameters, were obtained using the `valence` routine in the Tinker program (v. 8.4.2),[8] taking as input harmonic frequencies at the ωB97X-D/6-311+G* level. Force field parameters are included in a separate document.

S1.2 Simulation Details

Molecular dynamics (MD) simulations were performed using the Tinker-HP program.[9] Most simulations in isotropic water were performed using a cubic unit cell of dimensions 31.34 Å × 31.34 Å × 31.34 Å containing 1,024 water molecules plus a single ion, corresponding to a density of 0.997 g/cm^3. All simulations were performed under NVT conditions at $T = 298$ K, using a Berendsen thermostat, with a real-space cutoff of 9.4 Å for Ewald summation. Convergence tests in a much smaller unit cell (18.80 Å × 18.80 Å × 18.80 Å, containing 222 water molecules at the same density) suggest that the smaller cell would have been adequate. For example, RDFs for NO_3^-, SO_4^{2-}, and PO_4^{3-} obtained in the smaller cell are indistinguishable (upon windowing to obtain a smooth RDF) from those computed using the larger cell; see Fig. S1.

For the bulk (isotropic) simulations, neat liquid water was first equilibrated for 1 ns. Following insertion of the ion, the system was equilibrated for another 500 ps prior to a second 500 ps production run, with snapshots extracted from the latter every 5 ps for subsequent analysis and electronic structure calculations. The I^-(aq) and SCN^-(aq) trajectories were extended to 1 ns of production simulation as these were used to establish the criteria for partitioning the periodic slab simulations into bulk and an interfacial parts, and we wanted to obtain good statistics even for narrow definitions of the interfacial region such as GDS − 1 Å in Fig. 3.

Figure S2 presents the complete set of X$\cdots$O$_w$ RDFs (in isotropic water) for each of the anions considered in this work. These are generally good agreement with published results for the same ions, *e.g.*, for iodide,[10] bromide,[11] cyanide,[12] sulfate,[13] chlorine oxyanions ClO_x^-,[14] nitrate,[15], nitrite,[16] phosphate,[17] thiocyanate,[18] and carbonate.[19] A detailed comparison of coordination numbers for aqueous nitrate is presented in Table S1, and the results are found to be in good agreement with three other MD simulations,[15,20,21] and with the coordination number inferred from x-ray scattering experiments.[22]

For sulfite (SO_3^{2-}) and for chlorate (ClO_3^-), however, we obtain an inner solvation shell at a smaller value of r that does not appear in previously-published work.[14,23] In these cases, our *second* peak in $g(r)$ coincides with the first peak in the published results. The inner peak that we obtain integrates to 2–3 water molecules, and integrating over both peaks recovers a coordination number similar to the first-shell coordination numbers reported in previous work. For example, the first two peaks in the S–O$_w$ RDF for SO_3^{2-}(aq) integrate to $\langle CN_2 \rangle = 12.6$ water molecules, as compared to 12.5 molecules contained in the first peak of the RDF reported in Ref. 23. For ClO_3^-, we obtain a coordination number $\langle CN_2 \rangle = 17.6$ (first two peaks) as compared to the value $\langle CN_1 \rangle = 11.1$ (first peak) that is reported in Ref. 14. The previous simulations of these two ions, in Refs. 14 and 23, use a "quantum-mechanical charge-field molecular dynamics" method,[24] an unusual form of QM/MM that is not widely used. In view of the favorable comparisons between the present simulations and published literature for the other ions, along with the consistent protocol that was used here to generate force field parameters for all of the ions that we consider, we are suspicious of artifacts in the simulations reported in Refs. 14 and 23. We have not attempted to investigate this further, however.

S1.3 Gibbs Dividing Surface

Periodic slab simulations were performed as described in Section S1.2, but using a 31.34 Å×31.34 Å×156.71 Å periodic simulation cell. The z axis serves as the surface normal vector, with the xy plane (*i.e.*, $z = 0$) taken to divide the initial cubic box into equal halves. To determine the position $z = z_{\mathrm{GDS}}$ of the Gibbs dividing surface (GDS), density profiles along the z axis were computing using histogram bin widths $\Delta z = 0.5$ Å. Following previous work,[25–29] these density data $\rho(z)$ were fit to the function

$$\rho(z) = \tfrac{1}{2}\bar{\rho}\Big(1 \pm \tanh\big[\beta(z - z_{\mathrm{GDS}})\big]\Big) \tag{S1}$$

where $\bar{\rho}$ denotes the bulk water density. Parameters for this fit are listed in Table S2 for each ion. The value $z = z_{\mathrm{GDS}}$ defines the midpoint of the switching region in Eq. (S1), at which point the density has fallen to half of its bulk value of $\bar{\rho}$. The parameter β defines the width of the interfacial region, which is $\approx 4/\beta$ according to Eq. (S1).

The distance parameter d_{GDS} that is used in this work is defined as the distance from the center of mass of the ion to the plane defined by $z = z_{\mathrm{GDS}}$, which defines the liquid/vapor interface. We take d_{GDS} to be a signed quantity with positive values indicating the liquid side of the interface. Negative values are encountered only occasionally (and transiently). This distance coordinate is plotted along the NO_3^-(aq) trajectory in Fig. S3. As observed also for I^-(aq) and SCN^-(aq) in Fig. 4(a), the nitrate ion moves back and forth between the interfacial region and the bulk-like interior of the slab, and this is observed regardless of whether the ion is initially located in the bulk region or at the air/water interface. The ClO_4^- and Br^- ions also move readily between the bulk and interfacial regions, whereas ions with higher charge density (including SO_4^{2-}, SO_3^{2-}, PO_4^{3-}, and CO_3^{2-}) stay away from the interface. For these and other ions, plots of $d_{\mathrm{GDS}}(t)$ along the trajectories can be found in Fig. S4.

We have considered I^-(aq) and SCN^-(aq) in detail as two examples of ions that exhibit significant surface activity. The fluctuating distance coordinate $d_{\mathrm{GDS}}(t)$ for these two ions is plotted in Fig. S5, which is the same data as in Fig. 4(a) but presented here alongside some snapshots from the MD trajectory. These snapshots document the fact that the ion is truly air-exposed at the interface, when d_{GDS} is smallest. Similarities in short-range hydrogen-bonding structure at the interface, as compared to bulk water, therefore cannot simply be explained as resulting from a residual water layer that protects the ion from the interface. Quantitative characterization of the short-range structure is discussed in the next section.

S1.4 Short-Range Structural Analysis

Hard ions are seldom found at the air/water interface but are included in our data set for completeness, and because they make for challenging tests of our protocol to compute aqueous-phase VIEs due to slower convergence with respect to explicit water in the case of polyvalent ions. Our short-range structural analysis will be limited to the monovalent ions, however. Table S3 presents the cutoffs that were used to determine the short-range structural metrics that are listed in Table 2. These metrics are specified in terms of geometrical parameters that are defined in Fig. S6.

First- and second-shell coordination numbers (CN_1 and CN_2) are defined by a single cutoff distance $r(XO_w)$, where O_w represents a water oxygen and X is the central atom of the ion, *e.g.*, X = Cl for ClO_n^- and X = C for SCN^-. The cutoff values $r(XO_w)$ are listed in Table S3 and are chosen differently for CN_1 versus CN_2. For the former, we take the cutoff to be equal to the location of the first minimum in the RDF for $X\cdots O_w$. That way, CN_1 counts the number of water molecules up to the traditional definition of the first solvation shell, for a simulation in bulk water, and we then use that same cutoff to compute CN_1 at the air/water interface. In the case of I^-(aq), however, the first minimum in $g(r)$ is extremely shallow [see Fig. S2(b)], indicative of a solvation structure that is not very well-defined beyond the first solvation shell. In this case, we set the cutoff $r(XO_w) = 4.5$ Å, following Ref. 30. The aqueous SCN^- and ClO_4^- ions also exhibit negligible structure beyond the first solvation shell. For these species, it makes little sense to define CN_2 in the same way as CN_1. Instead, we set CN_2 equal to the radius needed to converge the VIE calculations, for each of the anions considered here. The requisite radius is $r(XO_w) = 5.5$ Å for Cl^-,

6.5 Å for I^- and Br^-, and 6.0 Å for all of the other monovalent ions; these cutoffs are listed in Table S3. Polyvalent ions require a larger radius to converge the VIE but we do not analyze their solvation structure in detail because they do not exhibit surface activity.

To quantify the number of hydrogen bonds n_{HB}, we use a distance cutoff based on the donor–acceptor distance $r(AH_w)$, where A is the hydrogen-bond acceptor atom of the anion. (For example, A = O for the oxyanions ClO_n^- and NO_n^-.) Similar to the definition of CN_1 above, we set a distance cutoff equal to the first minimum in the RDF for $r(AH_w)$, which is different for each ion (see Table S3), but then combine this with an angular cutoff $\theta(H_wAO_w) \leq 30°$ that is the same for each ion. See Fig. S6 for geometric definitions of these structural parameters. For $I^-(aq)$, the cutoff distance (3.4 Å) and angle (30°) used here coincide with those used in a previous study of the same species,[31] where they were also selected based on examination of the relevant RDFs. Previous studies have reported incomplete separation of the first and second peaks in the $I^- \cdots O_w$ RDF,[31,32] which is attributed to a diffuse structure shell of the ion, and we obtain similar results. Examining the $I^- \cdots O_w$ RDF in Fig. S2, one observes a first maximum at 3.8 Å, versus values of 3.5–3.8 Å reported in previous simulations.[31,32] The RDF for $I^- \cdots H_w$ that we obtain exhibits a first maximum at 2.8 Å, as compared to values of 2.5–2.9 Å reported in previous work.

Table 2 tabulates short-range structural metrics for each of the monovalent ions, both in bulk water (taken from the isotropic simulations) and at the air/water interface (defined by GDS − 3 Å). The same data are also presented in the form of radar plots in Figs. 6, S7, and S8, which also compare the isotropic or "true bulk" result to that obtained from the interior region of the periodic slab. (These are found to be virtually identical, indicating that the slab is sufficiently wide to obtain bulk-like behavior in its interior.)

At the interface, the CN_1 and CN_2 metrics are noticeably different from their bulk values but this is expected, as it reflects the reduced liquid density in the interfacial region. Note that the $\beta \approx 0.6$ Å^{-1} for each of the soft ions (Table S2), which corresponds to an interfacial width $4/\beta \approx 6.7$ Å. The GDS lies at the midpoint of this region and therefore an interfacial region defined by GDS − 3 Å lies entirely within the region of density falloff from its bulk value. Other short-range structural parameters differ by modest amounts when comparing the bulk and interfacial regions of the periodic slab simulations. The $I^-(aq)$ and $ClO_4^-(aq)$ ions are each characterized by 0.8 fewer hydrogen bonds at the interface, relative to the bulk values $n_{HB} = 6.0$ (I^-) and $n_{HB} = 7.0$ (ClO_4^-). On the other hand, for $SCN^-(aq)$ and $NO_3^-(aq)$ the number of hydrogen bonds is reduced only by 0.1 and 0.2, respectively, at the air/water interface. Average hydrogen-bond distances ($\bar{r}_{HB}$) and angles ($\bar{\theta}_{HB}$) are not modified in any meaningful way in the interfacial region.

We also analyzed the orientation of the first solvation shell of $I^-(aq)$ and of $SCN^-(aq)$ with respect to the air/water interface, as this orientation has been examined previously for $I^-(aq)$,[30] revealing anisotropic orientation at the interface that largely averages away in bulk water. Following Ref. 30 (and extending that analysis to the case of SCN^-), we have examined the distribution of $\cos(\bar{\Theta}_{AO\perp})$, where the angle $\Theta_{AO\perp}$ is defined as

$$\Theta_{AO\perp} = \cos^{-1}\left(\frac{\mathbf{r}_{XO} \cdot \mathbf{r}_\perp}{\|\mathbf{r}_{XO} \cdot \mathbf{r}_\perp\|}\right) \tag{S2}$$

and $\bar{\Theta}_{AO\perp}$ represents its value averaged over each of the n_{HB} first-shell hydrogen bonds, (Note that A = I for iodide and A = N for thiocyanate.) The vector $\mathbf{r}_\perp$ indicates the surface normal. The distribution of values of $\cos(\bar{\Theta}_{AO\perp})$ are shown in Fig. S9, for several different partitions between the bulk and interfacial regions of the periodic slab simulations. The bulk distributions should be approximately isotropic, and this is clearly not the case when the interface is defined as GDS − 1 Å, suggesting that this choice mixes some anisotropic interfacial configurations into the bulk data, thus skewing the latter. The bulk distributions are much closer to being symmetric about $\cos(\bar{\Theta}_{AO\perp}) = 0$ for the GDS − 3 Å partition, and is unchanged if GDS − 5 Å is used instead. For that reason, GDS − 3 Å is used to evaluate the short-range structural metrics that are listed in Table 2 and plotted in Figs. 6 and S7. For any of these three choices of the bulk/interfacial partition, the distribution of $\cos(\bar{\Theta}_{AO\perp})$ for the interfacial ions exhibits clear anisotropy, as noted previously for $I^-(aq)$.[30] Thus, the existence of this anisotropy exists alongside—and is therefore not inconsistent with—similarity between the short-range structural metrics when the ion is in a bulk versus interfacial solvation environment.

A two-dimensional scatter plot of $\cos(\bar{\Theta}_{AO\perp})$ versus the VIE is provided in Fig. S10, demonstrating a lack of correlation between this orientational parameter and the VIE. Note that $\bar{\Theta}_{AO\perp}$ is the average of the

angles between $\mathbf{r}_{\mathrm{XO}}$ and $\mathbf{r}_{\perp}$ for all of the ion–water hydrogen bonds in a given snapshot, and since there is some possibility of information loss as a result of this averaging, we examine joint probability distributions of the VIE and $\cos(\Theta_{\mathrm{AO}\perp})$, in Fig. S11, for both I^-(aq) and SCN^-(aq), with the data partitioned into bulk and interfacial subsets. For demonstrative purposes, we use a GDS $-$ 1 Å criterion to define the interfacial region, for the purposes of Fig. S11, in order to make the interfacial data maximally anisotropic. Despite this, we observe no obvious correlation between $\cos(\Theta_{\mathrm{AO}\perp})$ and the VIE: slices through the two-dimensional distribution at a fixed value of $\Theta_{\mathrm{AO}\perp}$ afford essentially identical VIE distributions.

Wick and Xantheas[32] have examined the anisotropy of the solvation environment around I^-(aq) using classical MD simulations with polarizable force fields. They find that the solvation environment can be anisotropic even in bulk water, because the induced dipole moment of I^- lifts the spherical symmetry. They characterize the anisotropy in terms of "radial-angular distribution functions" (RADFs), which are joint distributions in $r_{\mathrm{IH}} \sin\Theta_{\mathrm{ind}}$ and $r_{\mathrm{IH}} \cos\Theta_{\mathrm{ind}}$ where Θ_{ind} is the angle between the I^- polarizable dipole moment vector and the $\mathrm{I}^- \cdots \mathrm{H_w}$ vector, $\mathbf{r}_{\mathrm{IH}}$. We have examined the same correlations, and RADFs defined in the same way are plotted in Fig. S12 for I^-(aq) in both the bulk and interfacial regions of the periodic slab simulation. As observed in Ref. 32, for interfacial I^-(aq) there is significant anisotropy in both the first and second solvation shells, evident in Fig. S12(b) from the fact that there are vanishingly few data points with $r_{\mathrm{IH}} \cos\Theta_{\mathrm{ind}} < 0$. The data in Fig. S12(b) use GDS $-$ 1 Å to define the interfacial region, and if this definition is extended to GDS $-$ 3 Å then anisotropy is lost in the second solvation shell, although preserved in the first shell. That is consistent with the situation for I^-(aq) in bulk water, for which the RADF is plotted in Fig. S12(a) using an interface definition of GDS $-$ 5 Å to maximally separate bulk from interfacial data. Even with this maximalist definition, anisotropy is preserved in the second solvation shell of I^-(aq) in bulk water. This analysis is completely consistent with that of Ref. 32, and the comparison is intended to demonstrate that similarities in short-range hydration structure between bulk and interfacial ions, which have been documented in the present work, are not inconsistent with previous analyses of the solvation structure of these ions.

S2 Electronic Structure Calculations

Whereas the Psi4 program was used for the multipole analysis need to parameterize the force field, all other electronic structure calculations were performed using Q-Chem, v. 5.3.[33]

S2.1 Methods, Basis Sets, and Benchmarks

To compute the correct ionized state of a hydrated ion $\mathrm{X}^-(\mathrm{H_2O})_n$, where the highest occupied molecular orbital (HOMO) often corresponds to a water MO and thus ionization of X^- corresponds to removing an electron from an orbital below the HOMO, we used a procedure described in previous work.[29] Briefly, the initial guess for the self-consistent field (SCF) calculation consists of a superposition of fragment (monomer) densities, one for each $\mathrm{H_2O}$ molecule and another for the ionized solute, X. We then employ the maximum overlap method[34,35] (MOM) to converge a fully-relaxed SCF solution that resembles the guess occupancies, in the sense that the "hole" (below the HOMO level) is localized mainly on X.

VIEs for the aqueous ions that are reported in Fig. 2 and Table 2 were computed using the ωB97M-V density functional.[36] We use the aug-cc-pVTZ basis set for the ions, or aug-cc-pVTZ-PP (in conjunction with the eponymous effective core potential) for iodine and bromine, which is likely very close to the basis-set limit for DFT calculations. (Some calculations with double-ζ basis sets will be presented in Section S2.4, and these are found to be quite close to the triple-ζ results, which speaks to the convergence of the latter.) For the explicit water molecules we use the 6-31+G* basis set. A convergence threshold of 10^{-5} E_h was used for the SCF calculations, with other thresholds (integral screening and shell-pair formation) set at 10^{-8} a.u. A more complete discussion of VIE calculations, including their performance in conjunction with different solvation models, is deferred until Section S2.4.

In Section S2.4, we will also report some calculations at the level of second-order Møller-Plesset perturbation theory (MP2), within the resolution-of-identity (RI) approximation. Note, however, that artifactual

symmetry breaking in the Hartree-Fock wave function is a known problem for NO_3 radical,[37] and we encountered similar problems for NO_2 as well. This is considered in detail in Section S2.2, but in short the symmetry-breaking is often substantially mitigated by the use of density functional theory (DFT),[38,39] and we find that to be the case here. For this reason the MP2 calculations were not pursued to any significant extent.

Calculations for the ionized radicals are performed using a spin-unrestricted formalism. Values of $\langle \hat{S}^2 \rangle$ for each of the ions (corresponding to the VIE calculations reported in Table 2) are provided in Table S4, where the values are ensemble averages over each MD trajectory. In all cases $\langle \hat{S}^2 \rangle < 0.77$ (in atomic units), which should be compared to $\langle \hat{S}^2 \rangle = 0.75$ for a spin-pure doublet state. These results indicate that spin contamination is not a serious problem for these calculations.

Another possible source of error in DFT calculations of aqueous radicals is spin delocalization onto the surrounding solvent.[40,41] Table S5 reports the spin charge on each ionized radical, defined by Mulliken charge analysis applied to the spin density $\rho_\alpha - \rho_\beta$, averaged over the MD trajectories used to compute the VIEs. For comparison, both Hartree-Fock and ωB97M-V values are reported. At the Hartree-Fock level the unpaired electron is localized on the radical and the "spin leakage"[41] is no more than $0.05e$ (in the case of CN radical), and usually more along the lines of 0.02–0.03e. The spin leakage is only slightly larger at the DFT level but amounts to $< 0.1e$ in most cases. The largest spin leakage is only $0.13e$ (Cl^-) and $0.14e$ (ClO_3^-) in the largest cases.

To examine whether this level of spin delocalization represents a problem, we present benchmark calculations to assess the accuracy of the chosen DFT level of theory. As compared to the VIEs that are the main targets in this work, *adiabatic* ionization energies (AIEs) of gas-phase ions provide for straightforward comparison to experiment, because it is not necessary to consider vibrational states or Franck-Condon factors. An extensive database of AIEs can be found in Ref. 42 but we focus on the monovalent ions that are considered in this work. (Polyvalent ions are generally not stable in the gas phase.[43,44]) Experimental AIEs for these ions are listed in Table S6 and compared to ωB97M-V/aug-cc-pVTZ results, both with and without harmonic zero-point corrections. (The effect of zero-point corrections on the 0–0 transition energies is almost negligible, as it is also in adiabatic excitation energies of small molecules.[45–47]) The ωB97M-V/aug-cc-pVTZ calculations for the AIEs agree with experiment to within and average error of < 0.1 eV.

Adding water molecules to the picture, we compare against CCSD(T) calculations of VIEs for some small hydrated ion clusters, in Table S7. These VIEs are computed using the basis set that we use for the production-level VIEs, namely, aug-cc-pVTZ for the ion and 6-31+G* for the water molecules. CCSD(T) and ωB97M-V values of the VIEs are within 0.05 eV of one another. Thus, our selected level of electronic structure theory agrees with gas-phase results (both experiment and high-level theory) to within 0.1 eV. The 0.2–0.3 eV discrepancies that we observe with respect to liquid microjet experiments (Table 1) likely originates in the description of solvation effects, a part of which is associated with the vagaries of trying to compare the peak height in a VIE distribution to the band maximum in a photoelectron spectrum, which fundamentally entails a classical description of the effects of vibrational structure on the spectrum.

S2.2 Stability Analysis

The gas-phase nitrate radical is a notorious Jahn-Teller system,[48] and also a well-known symmetry-breaking problem in Hartree-Fock theory,[37,38] meaning that naïve optimization of the Hartree-Fock wave function for NO_3 often lands on a saddle point in the space of MO coefficients. Indeed, for hydrated clusters $NO_3(H_2O)_N$, corresponding to geometries of $NO_3^-(H_2O)_N$ extracted from MD simulations, we find that the Hartree-Fock solution obtained using Q-Chem's default SCF algorithm (superposition of atomic densities guess and direct inversion in the iterative subspace) almost *always* lands on an unstable solution, as demonstrated by subsequent wave function stability analysis. In such cases, we perturb the MOs along the lowest eigenmode of the orbital Hessian (corresponding to the most negative eigenvalue and the direction of energy lower in MO space), then re-converge the solution using geometric direct minimization.[49] The energy lowering thus obtained ranges from 1–3 eV and is plotted in Fig. S13, for snapshots along an MD trajectory of NO_3^-(aq). The VIE computed at the MP2 level is rather erratic for NO_3^-(aq) because the stable and unstable Hartree-Fock solutions have rather different correlation energies. We observe similar (though somewhat less pervasive)

symmetry-breaking problems in the case of NO_2. For this reason, no MP2-level VIEs are reported for either NO_2^- or NO_3^- in Table S9.

DFT is often found to mitigate symmetry breaking in the region of equilibrium geometries.[38,39] Results of the same stability analysis that was applied to the Hartree-Fock solutions for $NO_3(H_2O)_N$ was applied at the DFT level using three different functionals, with results (in the form of energy lowering, as in Fig. S13) shown in Fig. S14. The B3LYP functional occasionally lands on solutions that lie 1–6 eV above a lower-energy SCF solution, which is even larger than what was obtained at the Hartree-Fock level, although many of the B3LYP data points also result in energy lowering of $\lesssim 1$ eV. In contrast, for the ωB97X-D functional[50] most of the stabilization energies are < 1 eV and some are zero, indicating that the original SCF solution that was obtained using default convergence parameters is, in fact, a stable solution. This is true even more so for results obtained using the ωB97M-V functional.[36] For this reason, we have opted to use ωB97M-V for the VIE computations that we put up against experiment.

It remains the case, however, that many of the SCF solutions for $NO_3(H_2O)_N$ that are obtained using the ωB97M-V functional are unstable. To carry out stability analysis at every single snapshot is problematic or at least time-consuming and we have only performed spot-checks on other ions; however, only for NO_3 and NO_2 do we detect any problems with unstable SCF solutions. (We note that stability of the SCF solutions does not appear to have been considered in previous periodic DFT calculations of the VIEs for the same data set of ions that is examined here.[51]) VIEs obtained using the ωB97X-D and ωB97M-V functionals exhibit very similar fluctuations along the MD trajectory, as shown in Fig. S15.

S2.3 Continuum Solvation Models

Nonequilibrium continuum boundary conditions, for both isotropic and interfacial environments, were implemented using state-specific Poisson boundary conditions, as implemented in the Poisson Equation Solver (PEqs) developed by Coons and Herbert.[29] (We use the "W-cycle" multigrid algorithm that is described in Ref. 29.) The PEqS algorithm presented in Ref. 29 is itself an improvement upon the version originally developed in Ref. 28 and improves the stability of the original version by using the polarization potential (rather than the polarization charge density) as the quantity that is iterated to convergence. Relative to the algorithm presented in Ref. 29, the present version of PEqS is further improved by eliminating Gaussian blurring of the nuclear charges, which was a holdover from the older (less stable) version of the algorithm.[52] The electrostatic potentials from both nuclei and electrons are treated exactly (up to discretization on a grid) in the present version of PEqS.

Electrostatic potentials, charge densities, and the permittivity function $\varepsilon(\mathbf{r})$ were computed on a Cartesian grid using a spacing $\Delta x = \Delta y = \Delta z = 0.25$ Å. Both the spacing and the overall spatial extent of this grid were tested for convergence, as in previous work.[29] The permittivity function was constructed using a solvent accessible surface[53,54] (SAS) to delineate the boundary between the atomistic QM region and the continuum solvent, using Bondi's atomic radii,[55] although with the radius for hydrogen reduced to 1.1 Å as suggested in Ref. 56. The solvent probe radius used to construct the SAS is set to 1.4 Å, a standard value for water.[53,54] The permittivity $\varepsilon(\mathbf{r})$ is then switched smoothly between limiting values $\varepsilon = 1$ (inside the cavity) and $\varepsilon = 78$ (in bulk solvent), over a narrow window centered on the SAS around the ion–water cluster that constitutes the atomistic QM region. Examples of the permittivity function for both bulk and interfacial solvation are shown in Fig. S16.

To gauge the number of explicit water molecules needed to converge the VIE, convergence tests were performed using nonequilibrium IEF-PCM boundary conditions[57] in isotropic bulk water. The ion–water clusters that are used as solutes range in size from 4.5–7.5 Å in radius and water molecules within a specified radius of the ion are drawn from MD simulations. Atomic spheres that make up the SAS cavity surface are discretized using 302 Lebedev grid points per sphere.[58] Convergence tests of the VIE for NO_3^-(aq) are shown in Fig. 1 and for other ions in Fig. S17. Based on these convergence tests, we selected a QM radius of 7.0 Å for the polyvalent ions, 6.5 Å for Br^- and I^-, and 6.0 Å for the remaining monovalent ions. Tables S9 and 1 list the average number of water molecules $\langle N_{H_2O} \rangle$ corresponding to these radii, averaged over all of the snapshots used to compute the VIE in bulk water. These values are for the calculations in bulk water, as we assume that the same radii are sufficient to converge the interfacial VIEs as well. The veracity of

this assumption is supported by the similarities between bulk and interfacial VIEs and the fact that these similarities are stable with respect to modest variations in how the periodic slab simulations are partitioned into bulk and interfacial parts.

Table S8 presents a breakdown of the VIE computed for NO_3^-(aq) into an atomistic QM part (ΔU) and a continuum contribution (ΔG_{elst}),

$$\text{VIE} = \Delta U + \Delta G_{\text{elst}} \ , \tag{S3}$$

which is presented in Table S8 as a function of the radius of the atomistic QM region. The QM contribution

$$\Delta U = E[NO_3(H_2O)_N] - E[NO_3^-(H_2O)_N] \tag{S4}$$

represents the change in the internal energy of the $NO_3^-(H_2O)_N$ solute upon ionization of NO_3^-, whereas ΔG_{elst} is the change in the continuum solvation energy (electrostatic or polarization energy) upon ionization. From Table S8, one observes a decrease in the solvation contribution ΔG_{elst} as the solute encompasses more and more explicit water. This can be understood in terms of the Born ion model,[54] which predicts a $\sim 1/R$ decrease in the solvation energy G_{elst} as a function of the cavity radius, R. In the present calculations, the solvation energy G_{elst} of the (roughly spherical) $NO_3^-(H_2O)_N$ solute also decreases roughly as $\sim 1/R$ with respect to the radius R of the atomistic region, as shown in Fig. S18. Since G_{elst} is much larger for the negatively-charged initial state than it is for the $NO_3(H_2O)_N$ final state, the ΔG_{elst} data in Table S8 are dominated by this Born-like effect. Operationally, as the cluster radius increases, more and more of the solvation energy of NO_3^- is shifted into the atomistic QM region and out of the continuum part, as the charge on the ion is screened from the continuum by the presence of explicit water molecules. Nevertheless, $\Delta G_{\text{elst}} > 1$ eV even for $R = 7.5$ Å, so the continuum contribution is essential to our ability to obtain converged results with an affordable number of explicit water molecules.

S2.4 Detailed Analysis of the VIE Calculations

Results of the VIE calculations with are presented in Table S9. The data presented in Table 1 represent a subset of those in Table S9, corresponding to ωB97M-V with triple-ζ basis sets and the PEqS solvation model. For brevity, the uncertainties were omitted from Table 1 but are provided in Table S9, where they represent one standard deviation. Several different basis sets and solvation models are compared in Table S9. The column labeled "PCM" uses a nonequilibrium formulation[57,59] of a polarizable continuum model (PCM),[54,58] specifically the "integral equation formulation" (IEF-) PCM.[54,60] In most cases, the level of QM theory is DFT with ωB97M-V functional, using either the aug-cc-pVDZ or aug-cc-pVTZ basis set to describe the ion, with 6-31+G* used to describe the water molecules. The SG-2 quadrature grid is used for all DFT calculations.[61]

We also considered MP2 calculations, with aug-cc-pVDZ for the ion and 6-31+G* for the water. However, due to problems with stability of the Hartree-Fock wave functions (as described in Section S2.2), we did not attempt to push the MP2 calculations to larger basis sets, and errors in the VIEs at the MP2/double-ζ level are considerably larger than those at the ωB97M-V/triple-ζ level. As such, the DFT approach was used for all of the production-level calculations reported here. That said, in the the long term we see the ability of our *aperiodic* VIE protocol to be used with correlated wave functions as a significant advantage relative to periodic DFT approaches to compute the same quantity.[51]

PCM solvation is appropriate for bulk water only, but makes a useful point of comparison to PEqS calculations in bulk water, and both sets of calculations (at the ωB97M-V/triple-ζ level of theory) are reported in Table S9. For ions in bulk water, the mean absolute deviation (MAD) between VIEs computed with PCM versus PEqS boundary conditions is a mere 0.16 eV, which is slightly smaller than the MAD of either data set with respect to experiment, indicating that these two approaches afford an equally valid description of ionization in bulk water. Only the PEqS approach, however, is extensible to interfacial solvation. Looking at the PEqS results using the ωB97M-V functional, we find that the choice of aug-cc-pVDZ versus aug-cc-pVTZ for the ion modifies the VIEs by an average of only 0.06 eV, suggesting that the ωB97M-V/triple-ζ results are likely nearly converged with respect to saturation of the basis set. Some

exploratory calculations suggest that increasing the basis set on the water molecules from 6-31+G* to 6-311+G* modifies VIEs by < 0.05 eV, while making the calculations prohibitively expensive for the cluster sizes that are needed to reach convergence.

Figure S19 plots the full distribution of VIEs obtained for I^-(aq) in both bulk water and at the air/water interface. The raw data are presented in the form of histograms, from which smooth curves are obtained via the kernel density estimation technique. (These are the same smooth curves that are plotted in Fig. 3.) It is clear from the raw data that the difference between the most probable VIE in bulk water and the most probably value at the air/water interface is smaller than the histogram bin width that we employ (0.25 eV, as dictated by our sampling statistics), and thus this difference is statistically insignificant given the data that we have. The choice of criterion for how to partition bulk from interfacial data (GDS $-$ 1 Å, GDS $-$ 3 Å, or GDS $-$ 5 Å) matters very little.

The corresponding raw histograms for all of the monovalent ions are provided in Fig. S20. (We do not consider the polyvalent anions because these do not spend enough time at the interface to obtain a good statistics.) We use GDS $-$ 3 Å as the partition criterion in most cases, although GDS $-$ 5 Å was used to obtain better statistics in a few cases where the ion spends less time near the air/water interface interface. The ClO^- ion does not enter the interior of the slab in our simulations (see Fig. S3), so GDS $-$ 1 Å was used in this case, in order to have some data the bulk region. As seen for I^-(aq) in Fig. S19, differences between the most probably VIE in the bulk versus the interfacial region of the slab are comparable to or smaller than the histogram bin width, meaning that they are not resolvable at this level of statistical sampling. Figure S21 converts these histograms into smooth distributions using the KDE technique and adds the distribution obtained from an isotropic bulk simulation; this is the analogue of Fig. 3 for the other surface-active ions.

Average bulk and interfacial VIEs obtained from these distributions are listed in Table S10. Relative to the periodic slab data presented in Table 1, the "interfacial" VIEs that are listed in Table S10 are averages only over the interfacial region of the slab, whereas the averages in Table 1 reflect the entire slab. Thus, the value in Table S10 is a better estimate of the true interfacial VIE, although in practice this distinction makes very little difference in most cases. Only for a few of the ions does the difference between the bulk VIE (obtained from an isotropic simulation with no air/water interface) and the true interfacial VIE (obtained from the topmost layers of a periodic slab calculation) exceed 0.1 eV, and two of those cases are polyvalent ions for which we have relatively little interfacial data because the ion spends very little time near the air/water interface. Three of the monovalent ions (CN^-, SCN^-, and ClO_3^-) do exhibit VIEs that are 0.2 eV smaller at the interface than in bulk water, but the difference in all other cases is < 0.1 eV. Bearing in mind that the standard deviations on the thermal distribution of VIEs are ≥ 0.3 eV (Table S9), the latter differences seem entirely negligible and even differences of 0.2 eV are unlikely to be resolvable experimentally, given the magnitude of the thermal fluctuations.

References

[1] P. Ren and J. W. Ponder, "Temperature and pressure dependence of the AMOEBA water model", *J. Phys. Chem. B* **108**, 13427–13437 (2004).

[2] A. Grossfield, P. Ren, and J. W. Ponder, "Ion solvation thermodynamics from simulation with a polarizable force field", *J. Am. Chem. Soc.* **125**, 15671–15682 (2003).

[3] D. S. Lambrecht, G. N. I. Clark, T. Head-Gordon, and M. Head-Gordon, "Exploring the rich energy landscape of sulfate-water clusters $SO_4^{2-}(H_2O)_{n=3-7}$: An electronic structure approach", *J. Phys. Chem. A* **115**, 11438–11454 (2011).

[4] P. Ren, C. Wu, and J. W. Ponder, "Polarizable atomic multipole-based molecular mechanics for organic molecules", *J. Chem. Theory Comput.* **7**, 3143–3161 (2011).

[5] K. A. Carter-Fenk, K. Carter-Fenk, M. E. Fiamingo, H. C. Allen, and J. M. Herbert, "Vibrational exciton delocalization precludes the use of infrared intensities as proxies for surfactant accumulation on aqueous surfaces", *Chem. Sci.* (in press; DOI: 10.1039/D1SC01276B).

[6] A. J. Stone, "Distributed multipole analysis: Stability for large basis sets", *J. Chem. Theory Comput.* **1**, 1128–1132 (2005).

[7] J. M. Turney, A. C. Simmonett, R. M. Parrish, E. G. Hohenstein, F. Evangelista, J. T. Fermann, B. J. Mintz, L. A. Burns, J. J. Wilke, M. L. Abrams, N. J. Russ, M. L. Leininger, C. L. Janssen, E. T. Seidl, W. D. Allen, H. F. Schaefer, R. A. King, E. F. Valeev, C. D. Sherrill, and T. D. Crawford, "Psi4: An open-source *ab initio* electronic structure program", *WIREs Comput. Mol. Sci.* **2**, 556–565 (2012).

[8] J. A. Rackers, Z. Wang, C. Lu, M. L. Laury, L. Lagardère, M. J. Schnieders, J.-P. Piquemal, P. Ren, and J. W. Ponder, "Tinker 8: Software tools for molecular design", *J. Chem. Theory Comput.* **14**, 5273–5289 (2018).

[9] L. Lagardère, L.-H. Jolly, F. Lipparini, F. Aviat, B. Stamm, Z. F. Jing, M. Harger, H. Torabifard, G. A. Cisneros, M. J. Schneiders, N. Gresh, Y. Maday, P. Y. Ren, J. W. Ponder, and J.-P. Piquemal, "Tinker-HP: A massively parallel molecular dynamics package for multiscale simulations of large complex systems with advanced point dipole polarizable force fields", *Chem. Sci.* **9**, 956–972 (2018).

[10] V. T. Pham, I. Tavernelli, C. J. Milne, R. M. van der Veen, P. D'Angelo, C. Bressler, and M. Chergui, "The solvent shell structure of aqueous iodide: X-ray absorption spectroscopy and classical, hybrid QM/MM and full quantum molecular dynamics simulations", *Chem. Phys.* **371**, 24–29 (2010).

[11] S. Raugel and M. L. Klein, "An *ab initio* study of water molecules in the bromide ion solvation shell", *J. Chem. Phys.* **116**, 196–202 (2002).

[12] S. T. Moin and T. S. Hofer, "Hydration of the cyanide ion: An *ab initio* quantum mechanical charge field molecular dynamics study", *Phys. Chem. Chem. Phys.* **16**, 26075–26083 (2014).

[13] L. Pegado, O. Marsalek, P. Jungwirth, and E. Wernersson, "Solvation and ion-pairing properties of the aqueous sulfate anion: Explicit *versus* effective electronic polarization", *Phys. Chem. Chem. Phys.* **14**, 10248–10257 (2012).

[14] L. Eklund, T. S. Hofer, and I. Persson, "Structure and water exchange dynamics of hydrated oxo halo ions in aqueous solution using QMCF MD simulations, large angle x-ray scattering and EXAFS", *Dalton Trans.* **44**, 1816–1828 (2015).

[15] P. Banerjee, S. Yashonath, and B. Bagchi, "Coupled jump rotational dynamics in aqueous nitrate solutions", *J. Chem. Phys.* **145**, 234502 (2016).

[16] S. Vchirawongkwin, C. Kritayakornupona, A. Tongraar, and V. Vchirawongkwin, "Hydration properties determining the reactivity of nitrite in aqueous solution", *Dalton Trans.* **43**, 12164–12174 (2014).

[17] R. Costard, T. Tyborski, B. P. Fingerhut, and T. Elsaesser, "Ultrafast phosphate hydration dynamics in bulk H_2O", *J. Chem. Phys.* **142**, 212406 (2015).

[18] G. Tesei, V. Aspelin, and M. Lund, "Specific cation effects on SCN^- in bulk solution and at the air–water interface", *J. Phys. Chem. B* **122**, 5094–5105 (2018).

[19] S. Yadav and A. Chandra, "Structural and dynamical nature of hydration shells of the carbonate ion in water: An ab initio molecular dynamics study", *J. Phys. Chem. B* **122**, 1495–1504 (2018).

[20] L. X. Dang, T.-M. Chang, M. Roeselova, B. C. Garrett, and D. J. Tobias, "On NO_3^-–H_2O interactions in aqueous solutions and at interfaces", *J. Chem. Phys.* **124**, 066101 (2006).

[21] W. J. Xie, Y. I. Yang, and Y. Q. Gao, "Dual reorientation relaxation routes of water molecules in oxyanion's hydration shell: A molecular geometry perspective", *J. Chem. Phys.* **143**, 224504 (2015).

[22] R. Caminiti, G. Licheri, G. Paschina, G. Piccaluga, and G. Pinna, "Interactions and structure in aqueous $NaNO_3$ solutions", *J. Chem. Phys.* **72**, 4522–4528 (1980).

[23] L. Eklund, T. S. Hofer, A. B. Pribil, B. M. Rode, and I. Persson, "On the structure and dynamics of the hydrated sulfite ion in aqueous solution—an *ab initio* QMCF MD simulation and large angle x-ray scattering study", *Dalton Trans.* **41**, 5209–5216 (2012).

[24] T. S. Hofer, A. B. Pribil, B. R. Randolf, and B. M. Rode, "Ab initio quantum mechanical charge field molecular dynamics—a nonparameterized first-principle approach to liquids and solutions", *Adv. Quantum Chem.* **59**, 213–246 (2010).

[25] L. Frediani, R. Cammi, S. Corni, and J. Tomasi, "A polarizable continuum model for molecules at diffuse interfaces", *J. Chem. Phys.* **120**, 3893–3907 (2004).

[26] L. Frediani, B. Mennucci, and R. Cammi, "Quantum-mechanical continuum solvation study of the polarizability of halides at the water/air interface", *J. Phys. Chem. B* **108**, 13796–13806 (2004).

[27] M.-H. Ho, M. L. Klein, and I.-F. Kuo, "Bulk and interfacial aqueous fluoride: An investigation via first principles molecular dynamics", *J. Phys. Chem. A* **113**, 2070–2074 (2009).

[28] M. P. Coons, Z.-Q. You, and J. M. Herbert, "The hydrated electron at the surface of neat liquid water appears to be indistinguishable from the bulk species", *J. Am. Chem. Soc.* **138**, 10879–10886 (2016).

[29] M. P. Coons and J. M. Herbert, "Quantum chemistry in arbitrary dielectric environments: Theory and implementation of nonequilibrium Poisson boundary conditions and application to compute vertical ionization energies at the air/water interface", *J. Chem. Phys.* **148**, 222834 (2018).

[30] P. Jungwirth and D. J. Tobias, "Molecular structure of salt solutions: A new view of the interface with implications for heterogeneous atmospheric chemistry", *J. Phys. Chem. B* **105**, 10468–10472 (2001).

[31] J. M. Heuft and E. J. Meijer, "Density functional theory based molecular-dynamics study of aqueous iodide solvation", *J. Chem. Phys.* **123**, 094506 (2005).

[32] C. D. Wick and S. S. Xantheas, "Computational investigation of the first solvation shell structure of interfacial and bulk aqueous chloride and iodide ions", *J. Phys. Chem. B* **113**, 4141–4146 (2009).

[33] Y. Shao, Z. Gan, E. Epifanovsky, A. T. B. Gilbert, M. Wormit, J. Kussmann, A. W. Lange, A. Behn, J. Deng, X. Feng, D. Ghosh, M. Goldey, P. R. Horn, L. D. Jacobson, I. Kaliman, R. Z. Khaliullin, T. Kús, A. Landau, J. Liu, E. I. Proynov, Y. M. Rhee, R. M. Richard, M. A. Rohrdanz, R. P. Steele, E. J. Sundstrom, H. L. Woodcock III, P. M. Zimmerman, D. Zuev, B. Albrecht, E. Alguire, B. Austin, G. J. O. Beran, Y. A. Bernard, E. Berquist, K. Brandhorst, K. B. Bravaya, S. T. Brown, D. Casanova, C.-M. Chang, Y. Chen, S. H. Chien, K. D. Closser, D. L. Crittenden, M. Diedenhofen, R. A. DiStasio Jr., H. Do, A. D. Dutoi, R. G. Edgar, S. Fatehi, L. Fusti-Molnar, A. Ghysels, A. Golubeva-Zadorozhnaya, J. Gomes, M. W. D. Hanson-Heine, P. H. P. Harbach, A. W. Hauser, E. G. Hohenstein, Z. C. Holden, T.-C. Jagau, H. Ji, B. Kaduk, K. Khistyaev, J. Kim, J. Kim, R. A. King, P. Klunzinger, D. Kosenkov, T. Kowalczyk, C. M. Krauter, K. U. Lao, A. Laurent, K. V. Lawler, S. V. Levchenko, C. Y. Lin, F. Liu, E. Livshits, R. C. Lochan, A. Luenser, P. Manohar, S. F. Manzer, S.-P. Mao, N. Mardirossian, A. V. Marenich, S. A. Maurer, N. J. Mayhall, C. M. Oana, R. Olivares-Amaya, D. P. O'Neill, J. A. Parkhill, T. M. Perrine, R. Peverati, P. A. Pieniazek, A. Prociuk, D. R. Rehn, E. Rosta, N. J. Russ, N. Sergueev, S. M. Sharada, S. Sharma, D. W. Small, A. Sodt, T. Stein, D. Stück, Y.-C. Su, A. J. W. Thom, T. Tsuchimochi, L. Vogt, O. Vydrov, T. Wang, M. A. Watson, J. Wenzel, A. White, C. F. Williams, V. Vanovschi, S. Yeganeh, S. R. Yost, Z.-Q. You, I. Y. Zhang, X. Zhang, Y. Zhao, B. R. Brooks, G. K. L. Chan, D. M. Chipman, C. J. Cramer, W. A. Goddard III, M. S. Gordon, W. J. Hehre, A. Klamt, H. F. Schaefer III, M. W. Schmidt, C. D. Sherrill, D. G. Truhlar, A. Warshel, X. Xu, A. Aspuru-Guzik, R. Baer, A. T. Bell, N. A. Besley, J.-D. Chai, A. Dreuw, B. D. Dunietz, T. R. Furlani, S. R. Gwaltney, C.-P. Hsu, Y. Jung, J. Kong, D. S. Lambrecht, W. Liang, C. Ochsenfeld, V. A. Rassolov, L. V. Slipchenko, J. E. Subotnik, T. Van Voorhis, J. M. Herbert, A. I. Krylov, P. M. W. Gill, and M. Head-Gordon, "Advances in molecular quantum chemistry contained in the Q-Chem 4 program package", *Mol. Phys.* **113**, 184–215 (2015).

[34] A. T. B. Gilbert, N. A. Besley, and P. M. W. Gill, "Self-consistent field calculations of excited states using the maximum overlap method (MOM)", *J. Phys. Chem. A* **112**, 13164–13171 (2008).

[35] G. M. J. Barca, A. T. B. Gilbert, and P. M. W. Gill, "Simple models for difficult electronic excitations", *J. Chem. Theory Comput.* **14**, 1501–1509 (2018).

[36] N. Mardirossian and M. Head-Gordon, "ωB97M-V: A combinatorially optimized, range-separated hybrid, meta-GGA density functional with VV10 nonlocal correlation", *J. Chem. Phys.* **144**, 214110 (2016).

[37] W. Eisfeld and K. Morokuma, "A detailed study on the symmetry breaking and its effect on the potential surface of NO_3", *J. Chem. Phys.* **113**, 5587–5597 (2000).

[38] C. D. Sherrill, M. S. Lee, and M. Head-Gordon, "On the performance of density functional theory for symmetry-breaking problems", *Chem. Phys. Lett.* **302**, 425–430 (1999).

[39] U. Wille and T. Dreessen, "Mechanistic insights into $NO_3^\bullet$ induced self-terminating radical oxygenations, part 1: A computational study on $NO_3^\bullet$ and its addition to alkynes", *J. Phys. Chem. A* **110**, 2195–2203 (2006).

[40] A. J. Cohen, P. Mori-Sanchez, and W. Yang, "Insights into current limitations of density functional theory", *Science* **321**, 792–794 (2008).

[41] B. Rana and J. M. Herbert, "Role of hemibonding in the structure and ultraviolet spectroscopy of the aqueous hydroxyl radical", *Phys. Chem. Chem. Phys.* **22**, 27829–27844 (2020).

[42] J. C. Rienstra-Kiracofe, G. S. Tschumper, H. F. Schaefer, S. Nandi, and G. B. Ellison, "Atomic and molecular electron affinities: Photoelectron experiments and theoretical computations", *Chem. Rev.* **102**, 231–282 (2002).

[43] J. M. Herbert and J. V. Ortiz, "Ab initio investigation of electron detachment in dicarboxylate dianions", *J. Phys. Chem. A* **104**, 11786–11795 (2000).

[44] J. M. Herbert, "The quantum chemistry of loosely-bound electrons", in *Reviews in Computational Chemistry*, A. L. Parill and K. Lipkowitz, Eds., Vol. 28; Wiley-VCH: Hoboken, NJ, 2015; chapter 8, pages 391–517.

[45] R. Send, M. Kühn, and F. Furche, "Assessing excited state methods by adiabatic excitation energies", *J. Chem. Theory Comput.* **7**, 2376–2386 (2011).

[46] N. O. C. Winter, N. K. Graf, S. Leutwyler, and C. Hättig, "Benchmarks for 0–0 transitions of aromatic organic molecules: DFT/B3LYP, ADC(2), CC2, SOS-CC2 and SCS-CC2 compared to high-resolution gas-phase data", *Phys. Chem. Chem. Phys.* **15**, 6623–6630 (2013).

[47] P.-F. Loos and D. Jacquemin, "Evaluating 0–0 energies with theoretical tools: A short review", *ChemPhotoChem* **3**, 684–696 (2019).

[48] S. Mahapatra, W. Eisfeld, and H. Köppel, "Effects of multimode Jahn-Teller coupling on the photodetachment spectrum of nitrate anion (NO_3^-)", *Chem. Phys. Lett.* **441**, 7–15 (2007).

[49] T. Van Voorhis and M. Head-Gordon, "A geometric approach to direct minimization", *Mol. Phys.* **100**, 1713–1721 (2002).

[50] J.-D. Chai and M. Head-Gordon, "Long-range corrected hybrid density functionals with damped atom–atom dispersion corrections", *Phys. Chem. Chem. Phys.* **10**, 6615–6620 (2008).

[51] T. A. Pham, M. Govoni, R. Seidel, S. E. Bradforth, E. Schwegler, and G. Galli, "Electronic structure of aqueous solutions: Bridging the gap between theory and experiments", *Sci. Adv.* **3**, e1603210 (2017).

[52] S. K. Paul, M. P. Coons, and J. M. Herbert, "Erratum: 'Quantum chemistry in arbitrary dielectric environments: Theory and implementation of nonequilibrium Poisson boundary conditions and application to compute vertical ionization energies at the air/water interface"', *J. Chem. Phys.* **151**, 189901 (2019).

[53] A. W. Lange, J. M. Herbert, B. J. Albrecht, and Z.-Q. You, "Intrinsically smooth discretization of Connolly's solvent-excluded molecular surface", *Mol. Phys.* **118**, e1644384 (2020).

[54] J. M. Herbert, "Dielectric continuum methods for quantum chemistry", *WIREs Comput. Mol. Sci.* **11**, e1519 (2021).

[55] A. Bondi, "Van der Waals volumes and radii", *J. Phys. Chem.* **68**, 441–451 (1964).

[56] R. S. Rowland and R. Taylor, "Intermolecular nonbonded contact distances in organic crystal structures: Comparison with distances expected from van der Waals radii", *J. Phys. Chem.* **100**, 7384–7391 (1996).

[57] Z.-Q. You, J.-M. Mewes, A. Dreuw, and J. M. Herbert, "Comparison of the Marcus and Pekar partitions in the context of non-equilibrium, polarizable-continuum reaction-field solvation models", *J. Chem. Phys.* **143**, 204107 (2015).

[58] A. W. Lange and J. M. Herbert, "A smooth, nonsingular, and faithful discretization scheme for polarizable continuum models: The switching/Gaussian approach", *J. Chem. Phys.* **133**, 244111 (2010).

[59] J.-M. Mewes, Z.-Q. You, M. Wormit, T. Kriesche, J. M. Herbert, and A. Dreuw, "Experimental benchmark data and systematic evaluation of two *a posteriori*, polarizable-continuum corrections for vertical excitation energies in solution", *J. Phys. Chem. A* **119**, 5446–5464 (2015).

[60] A. W. Lange and J. M. Herbert, "Symmetric versus asymmetric discretization of the integral equations in polarizable continuum solvation models", *Chem. Phys. Lett.* **509**, 77–87 (2011).

[61] S. Dasgupta and J. M. Herbert, "Standard grids for high-precision integration of modern density functionals: SG-2 and SG-3", *J. Comput. Chem.* **38**, 869–882 (2017).

[62] U. Berzinsh, M. Gustafsson, D. Hanstorp, A. Klinkmüller, U. Ljungblad, and A.-M. Mårtensson-Pendrill, "Isotope shift in the electron affinity of chlorine", *Phys. Rev. A* **51**, 231–238 (1995).

[63] C. Blondel, P. Cacciani, C. Delsart, and R. Trainham, "High-resolution determination of the electron affinity of fluorine and bromine using crossed ion and laser beams", *Phys. Rev. A* **40**, 3698–3701 (1989).

[64] D. Hanstorp and M. Gustafsson, "Determination of the electron affinity of iodine", *J. Phys. B: At. Mol. Opt. Phys.* **25**, 1773–1783 (1992).

[65] S. E. Bradforth, E. H. Kim, D. W. Arnold, and D. M. Neumark, "Photoelectron spectroscopy of CN^-, NCO^-, and NCS^-", *J. Chem. Phys.* **98**, 800–810 (1993).

[66] M. K. Gilles, M. L. Polak, and W. C. Lineberger, "Photoelectron spectroscopy of the halogen oxide anions FO^-, ClO^-, BrO^-, IO^-, $OClO^-$, and OIO^-", *J. Chem. Phys.* **96**, 8012–8020 (1992).

[67] X.-B. Wang and L.-S. Wang, "The electronic structure and electron affinities of higher chlorine oxide radicals ClO_x ($x = 2$–4) from photoelectron spectroscopy of ClO_x^- anions", *J. Chem. Phys.* **113**, 10928–10933 (2000).

[68] K. M. Ervin, J. Ho, and W. C. Lineberger, "Ultraviolet photoelectron spectrum of NO_2^-", *J. Phys. Chem.* **92**, 5405–5412 (1988).

[69] A. Weaver, D. W. Arnold, S. E. Bradforth, and D. M. Neumark, "Examination of the $^2A_2'$ and $^2E''$ states of NO_3 by ultraviolet photoelectron spectroscopy of NO_3^-", *J. Chem. Phys.* **94**, 1740–1751 (1993).

[70] A. V. Marenich, C. J. Cramer, and D. G. Truhlar, "Universal solvation model based on solute electron density and on a continuum model of the solvent defined by the bulk dielectric constant and atomic surface tensions", *J. Phys. Chem. B* **113**, 6378–6396 (2009).

Figures & Tables

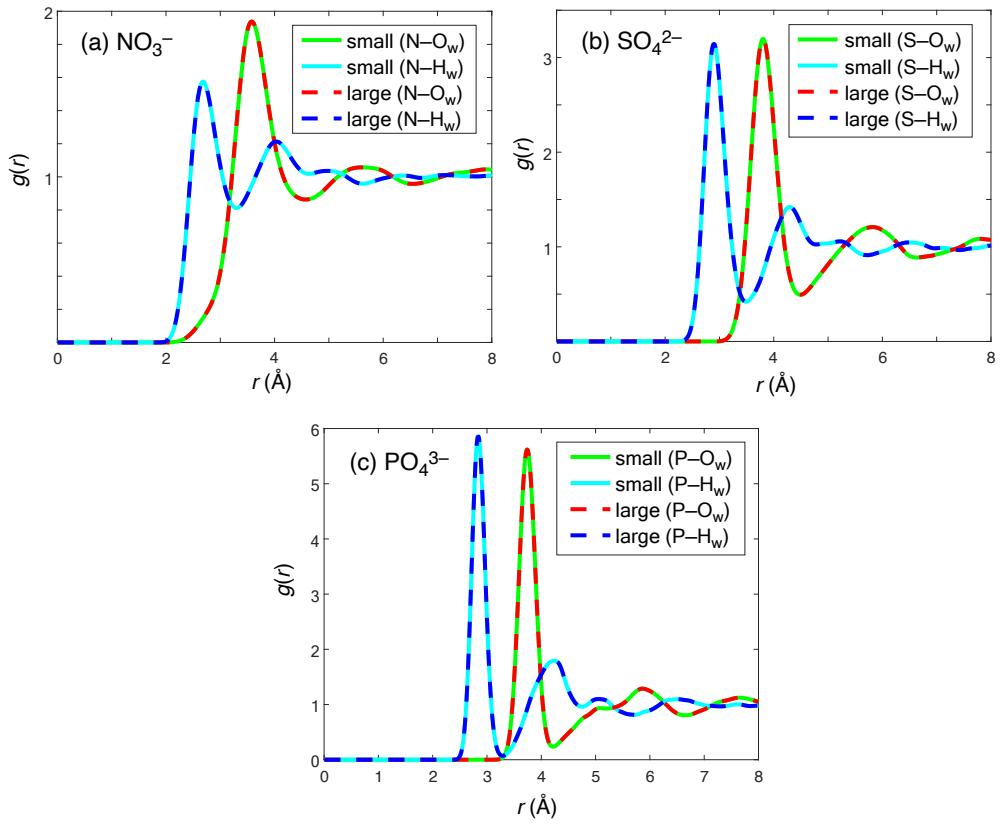

Figure S1: Comparison of RDFs for aqueous ions in a small simulation cell, $(18.80\ \text{Å})^3$ containing 222 water molecules, versus a larger simulation cell, $(31.34\ \text{Å})^3$ with 1,024 water molecules. Both sets of simulations use the same liquid density ($0.997\ \text{g/cm}^3$) and temperature (298 K). The structures are completely identical in both simulation cells.

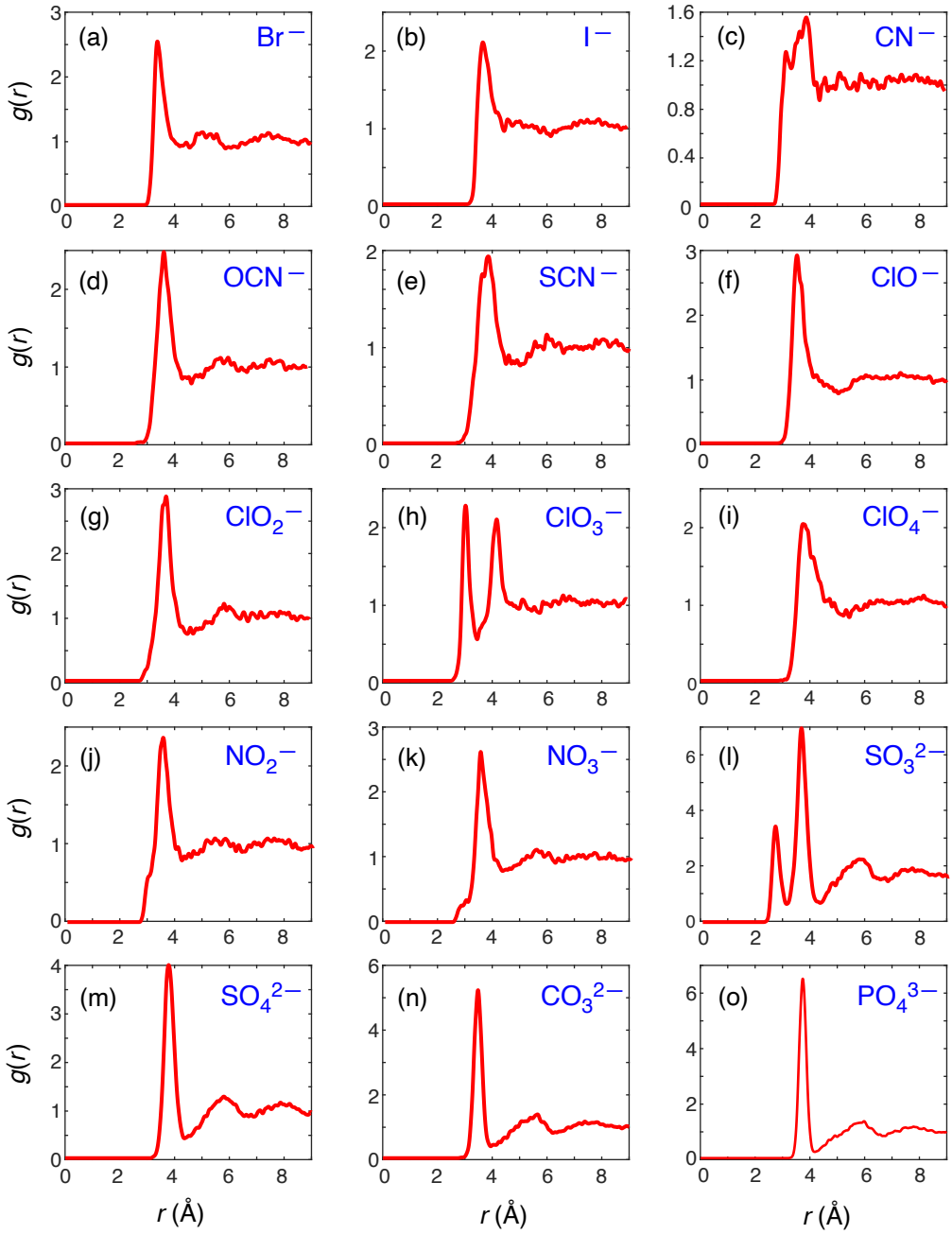

Figure S2: RDFs $g(r)$ for $\mathrm{X}\cdots\mathrm{O_w}$, where X represents the central atom of the ion and $\mathrm{O_w}$ is a water oxygen. These RDFs were obtained using 18.8 Å × 18.8 Å × 18.8 × Å isotropic simulation cells and the AMOEBA force field parameters developed as part of this work.

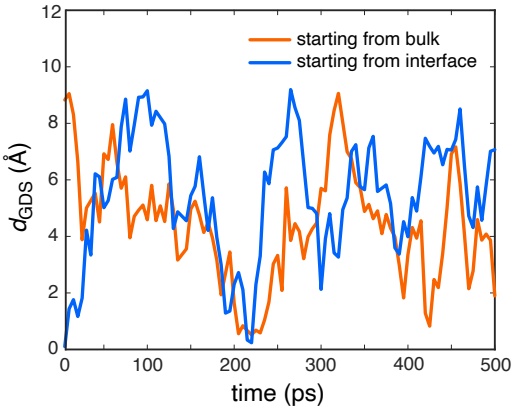

Figure S3: Instantaneous distance $d_{\mathrm{GDS}}(t)$ between the ion and the GDS for NO_3^-(aq), for a trajectory in a 18.8 Å $\times$ 18.8 Å $\times$ 94.0 Å periodic slab. (The distance d_{GDS} is computed with respect to the center of mass of the ion.) Irrespective of the starting point, the ion has a tendency to go back and forth between the interior of the slab and the interfacial region, however the ion stays strictly on the liquid side of the GDS ($d_{\mathrm{GDS}} > 0$) in this particular trajectory.

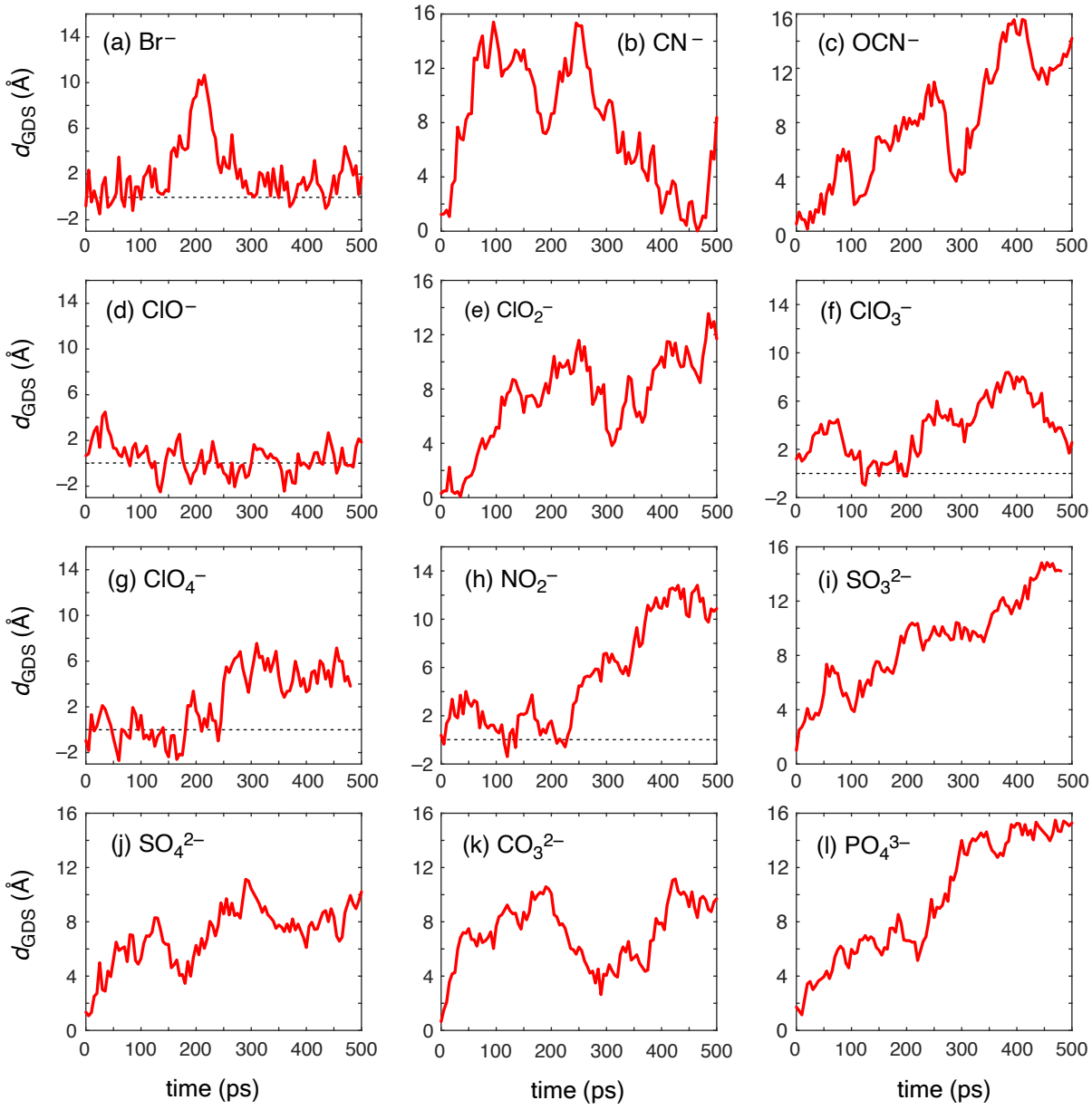

Figure S4: Instantaneous distance d_{GDS} from the ion to the GDS in the periodic slab simulations for various ions. Positive values of d_{GDS} indicate that the ion is on the liquid side of the GDS while negative values correspond to the vacuum side. The corresponding plots for I^-(aq) and SCN^-(aq) can be found in Fig. 4(a) and for NO_3^-(aq) it can be found in Fig. S3.

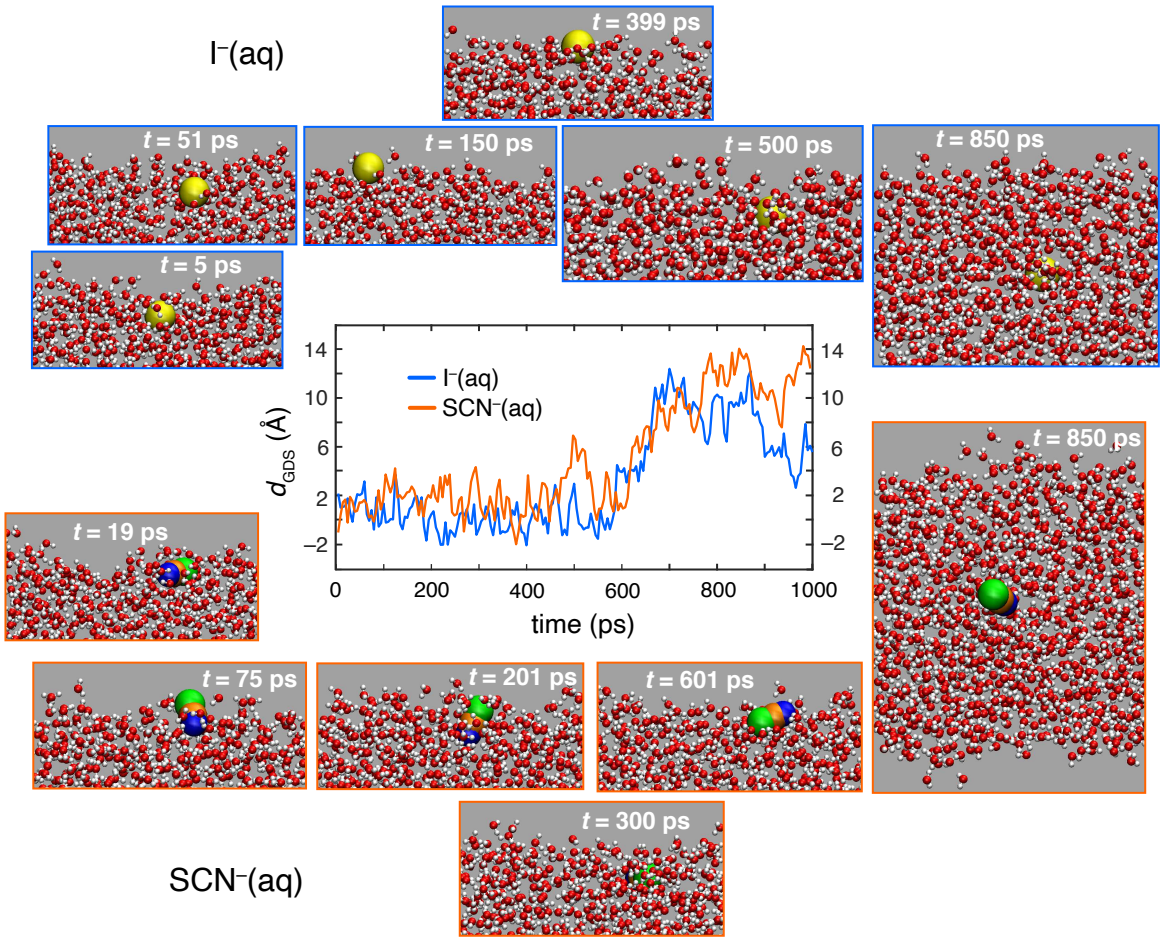

Figure S5: Top: snapshots from a periodic slab simulation of I^-(aq) at the air/water interface, with the ion shown as a van der Waals sphere. Bottom: snapshots from a periodic slab simulation of SCN^-(aq) at the air/water interface. Center: $d_{GDS}(t)$ for both trajectories, which is the same plot as Fig. 4(a).

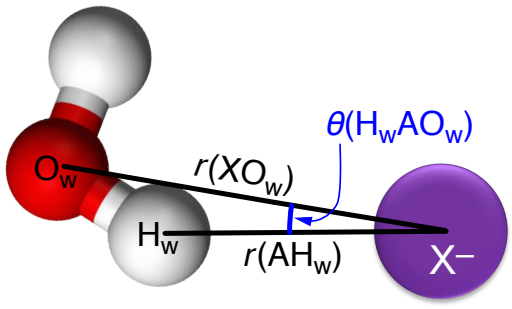

Figure S6: Distance and angle criteria for determining the hydration metrics CN_1, CN_2, and n_{HB}. Atom X is the central atom of the ion (*e.g.*, X = N for NO_3^- and take X = C for SCN^-). Atom A is the hydrogen bond acceptor atom (*e.g.*, A = O for NO_3^- and A = N for SCN^-).

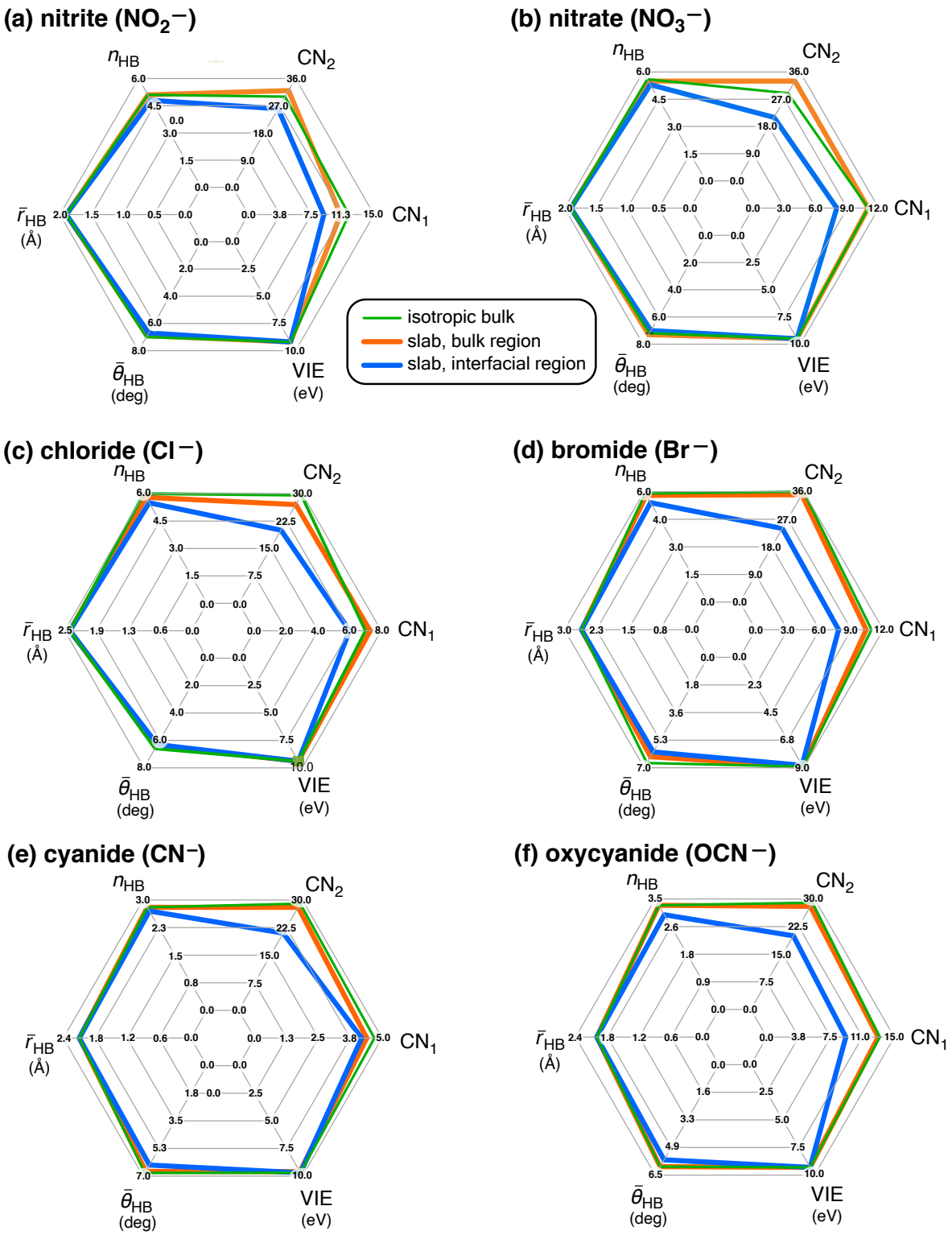

Figure S7: Radar plots comparing structural parameters of the local hydrogen-bonding network around various ions: NO_2^-, NO_3^-, Cl^-, Br^-, CN^-, and OCN^-. Results are shown for both isotropic bulk solution and for bulk and interfacial parts of a periodic slab simulation, partitioned according to GDS−3 Å. Numerical values for each of the structural parameters can be found in Table 2.

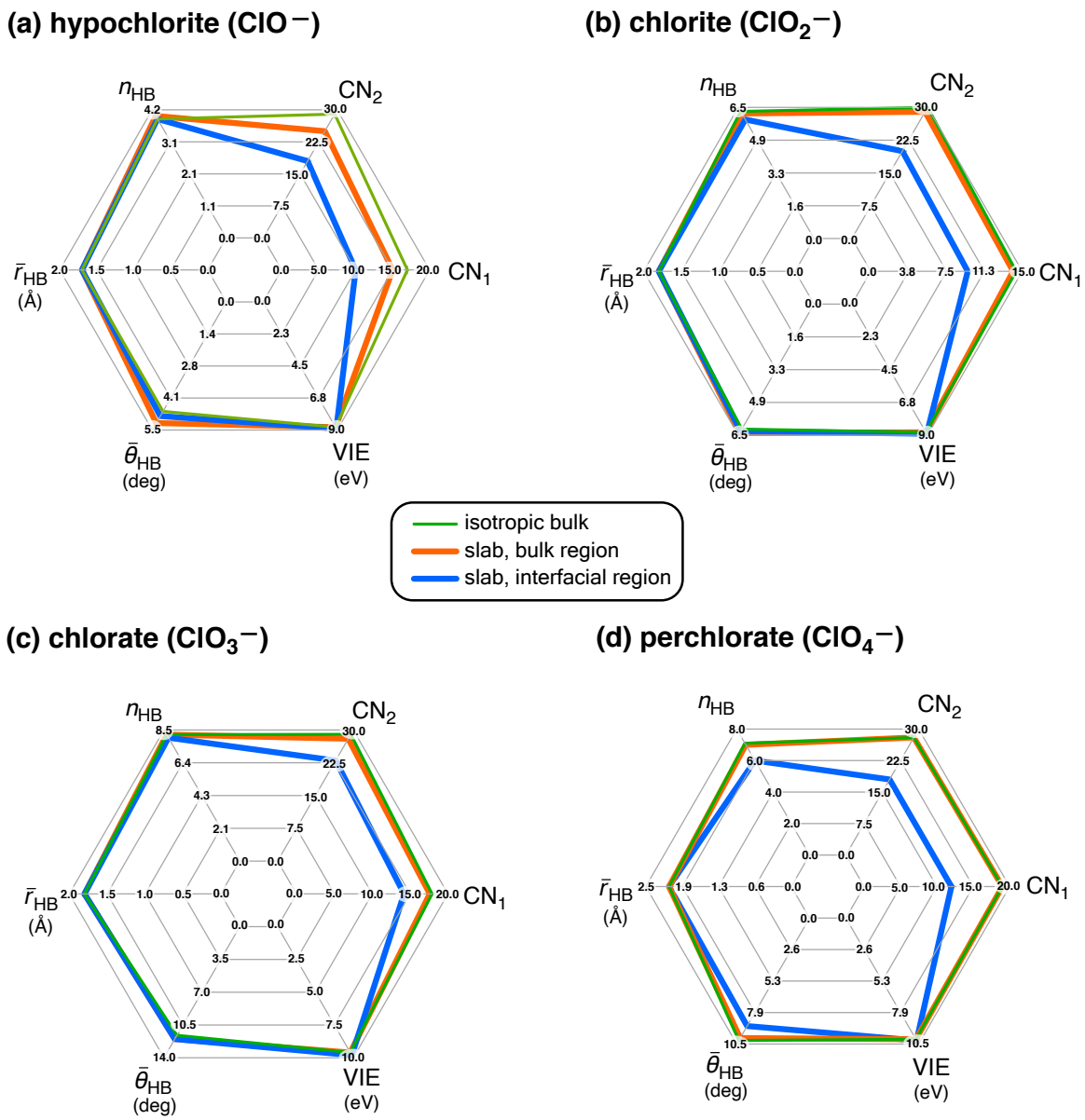

Figure S8: Radar plots comparing structural parameters of the local hydrogen-bonding network around ClO_n^- ions. Results are shown for both isotropic bulk solution and for bulk and interfacial parts of a periodic slab simulation, partitioned according to GDS − 3 Å. Numerical values for each of the structural parameters can be found in Table 2.

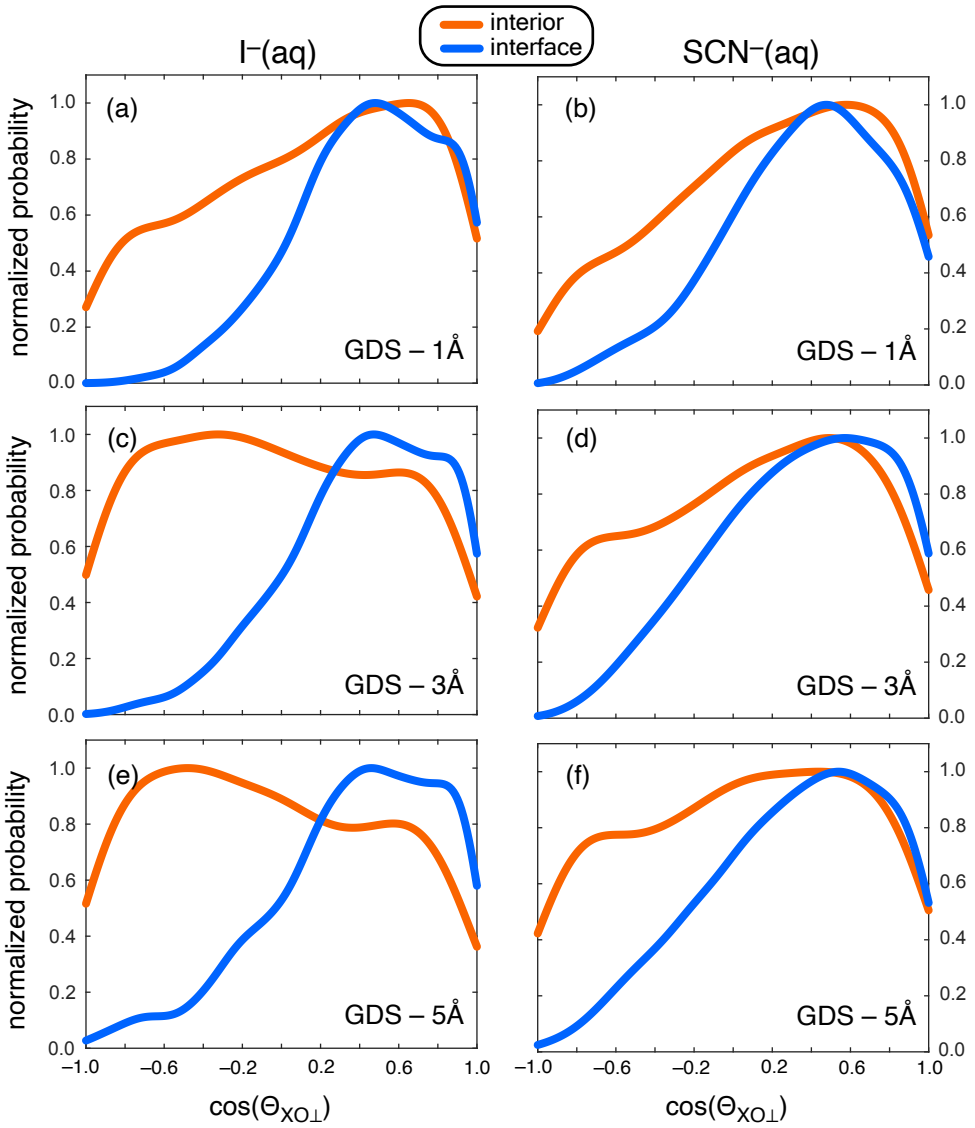

Figure S9: Distribution of $\cos(\bar{\Theta}_{\mathrm{AO}\perp})$, averaged over first-shell hydrogen bonds, with A = I for I^-(aq) and A = N for SCN^-(aq). These distributions, which were previously examined for I^-(aq) in Ref. 30, quantify the orientation of the ion–water hydrogen bonds with respect to the surface normal vector, with $\cos(\bar{\Theta}_{\mathrm{AO}\perp}) \approx 1$ indicating alignment. The upper, middle, and lower panels use three different dividing surfaces to partition the periodic slab data into interior and interfacial regions. A bulk-like environment ought to afford an isotropic distribution of angles, hence the data suggest that the GDS − 1 Å partition is a too-narrow definition of the interface, which mixes surface-oriented configurations into the interior region. For that reason, the GDS − 3 Å criterion is used in the short-range structural analysis, *e.g.*, in Table 2 and in Figs. 6 and S7.

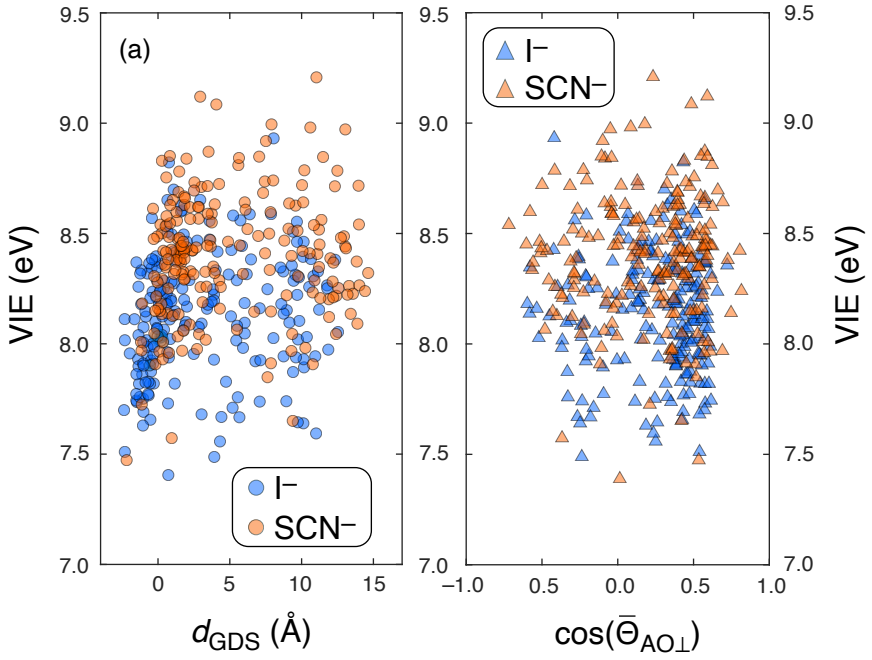

Figure S10: Scatter plots of VIEs computed for I^-(aq) and SCN^-(aq), versus (a) the distance from the ion to air/water interface, d_{GDS}; and (b) the average orientation of the hydrogen bonds with respect to the surface normal vector. Each data point represents a particular snapshot from an MD simulation, and $\bar{\Theta}_{AO\perp}$ in (b) is the average of the angles between the various $\mathbf{r}_{AO}$ vectors for the hydrogen bonds with the surface normal vector $\mathbf{r}_{\perp}$, for each of the ion–water hydrogen bonds. Panel (a) depicts the same data that are plotted in Fig. 5(a).

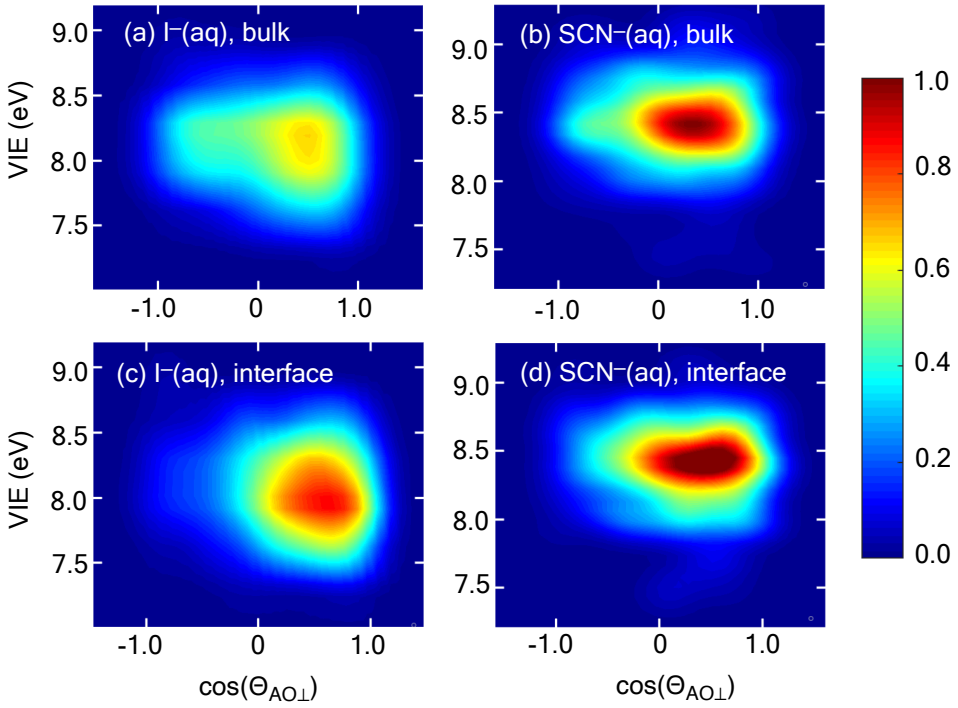

Figure S11: Joint distribution of the VIE and $\cos(\Theta_{\mathrm{AO}\perp})$ defined in Eq. (S2). The value of $\cos(\Theta_{\mathrm{AO}\perp})$ quantifies orientation of the ion–water hydrogen bonds with respect to the surface normal, with $\cos(\Theta_{\mathrm{AO}\perp}) \approx 1$ indicating alignment. Bulk and interfacial data are partitioned using the criterion GDS − 1 Å.

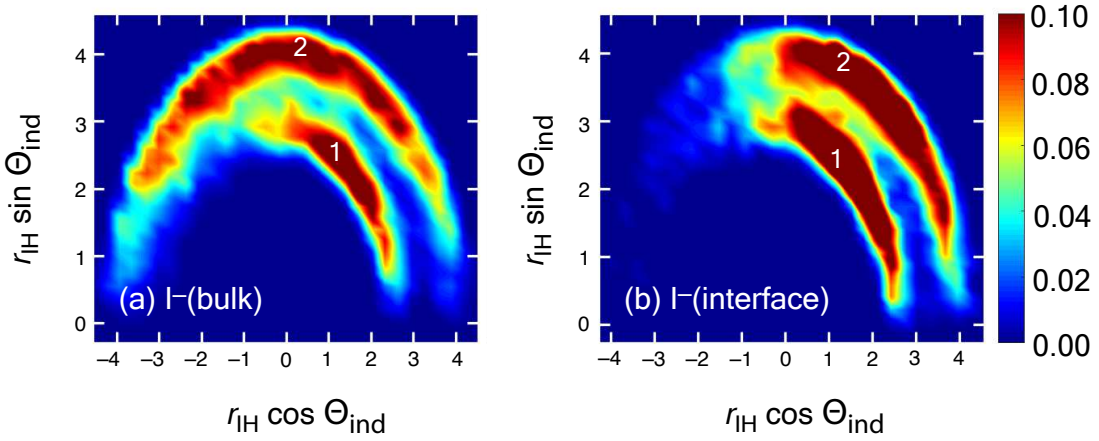

Figure S12: RADFs demonstrating anisotropy in the solvation structure around I^-(aq), both (a) in bulk water and (b) at the air/water interface. (To maximally separate bulk and interfacial structures, the former are defined using a partition of GDS − 5 Å and the latter using a partition of GDS − 1 Å.) The angle Θ_{ind} is that between the induced dipole moment vector of the ion and the hydrogen-bond vector $\mathbf{r}_{\mathrm{IH}}$, and all hydrogen bonds with $r_{\mathrm{IH}} \leq 4.5$ Å are included. Features labeled "1" and "2" correspond to the first and second solvation shells around the ion, respectively.

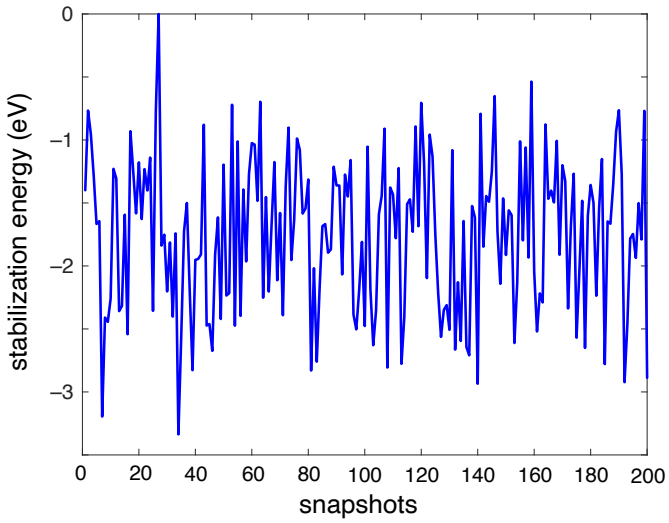

Figure S13: Results of stability analysis at the Hartree-Fock level, performed on hydrated clusters of NO_3 radical extracted from an MD simulation. Upon performing wave function stability analysis, the unstable wave function is perturbed along the lowest eigenmode of the orbital Hessian, and what is plotted is the energy lowering (stabilization energy) that is obtained. Negative values therefore indicate that the original SCF solution was unstable, and only for one snapshot did the Hartree-Fock solution obtained from the default SCF procedure turn out to be stable.

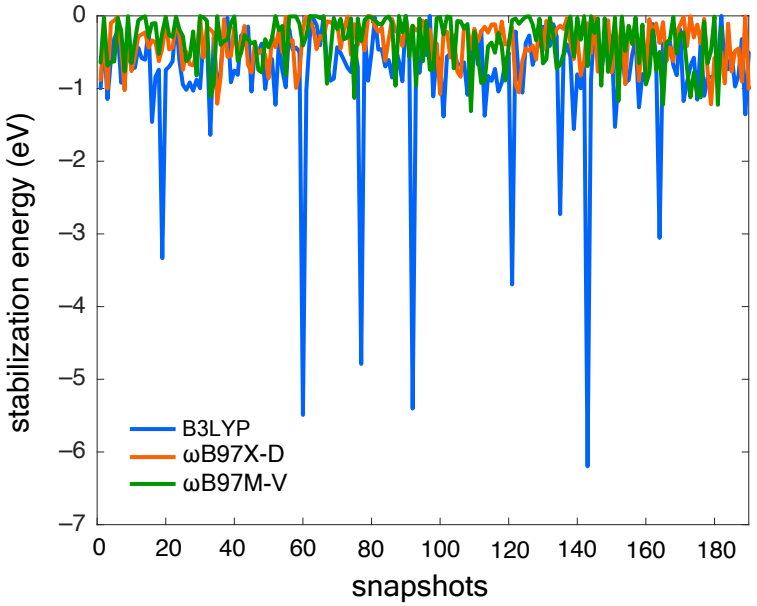

Figure S14: Results from Kohn-Sham stability analysis using three different density functionals, for hydrated NO_3 clusters. What is plotted is the energy lowering upon perturbing the SCF solution (obtained using the default SCF algorithm) in the direction of the lowest eigenmode of the orbital Hessian and re-converging the solution. (The corresponding Hartree-Fock data are plotted in Fig. S13.) A value of zero indicates that the original SCF solution was stable, as is the case for many (but certainly not all) of the snapshots at the ωB97M-V level.

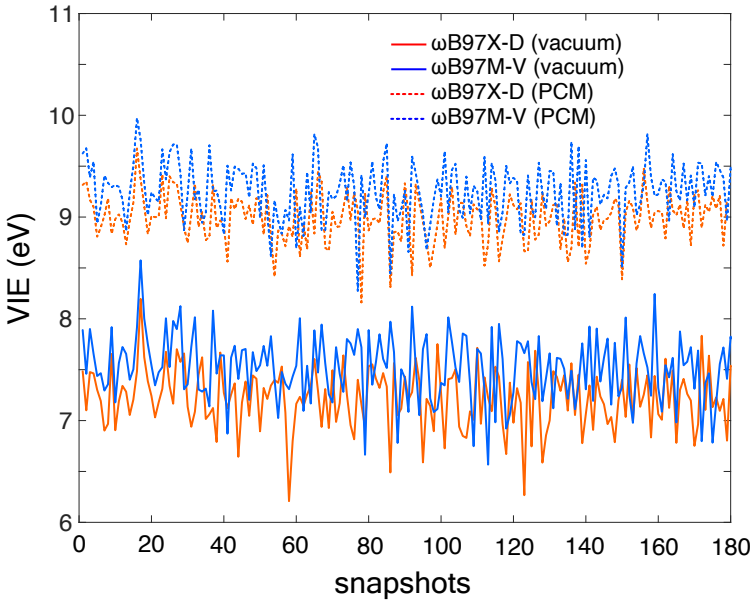

Figure S15: VIE calculations for NO_3^-(aq) with vacuum boundary conditions and with PCM boundary conditions, using two different functionals.

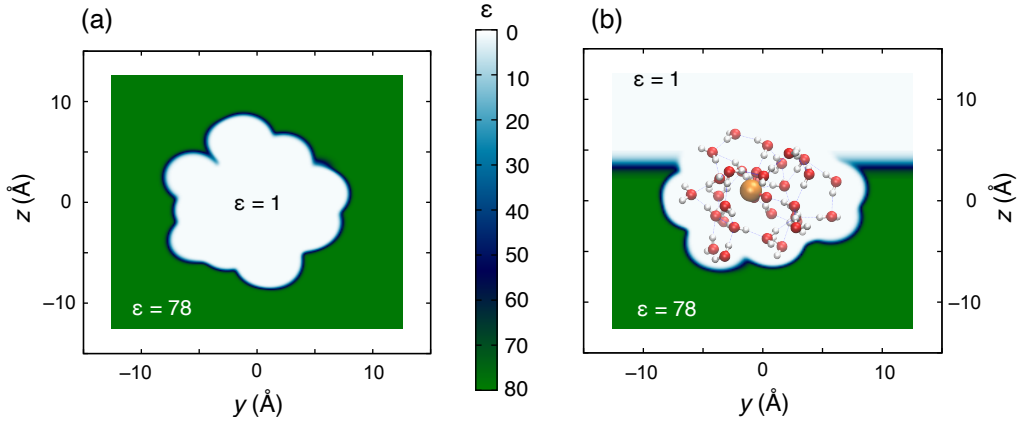

Figure S16: Illustration of the boundary conditions used in cluster-continuum calculations for (a) bulk water and (b) the air/water interface. The atomistic solute in this particular example is $ClO_3^-(H_2O)_{30}$, which is depicted in (b) The background color shows the function $\varepsilon(\mathbf{r})$, interpolating between $\varepsilon = 1$ above the Gibbs dividing surface (GDS) and $\varepsilon = 78$ below it, with $\varepsilon = 1$ inside of the solute cavity.

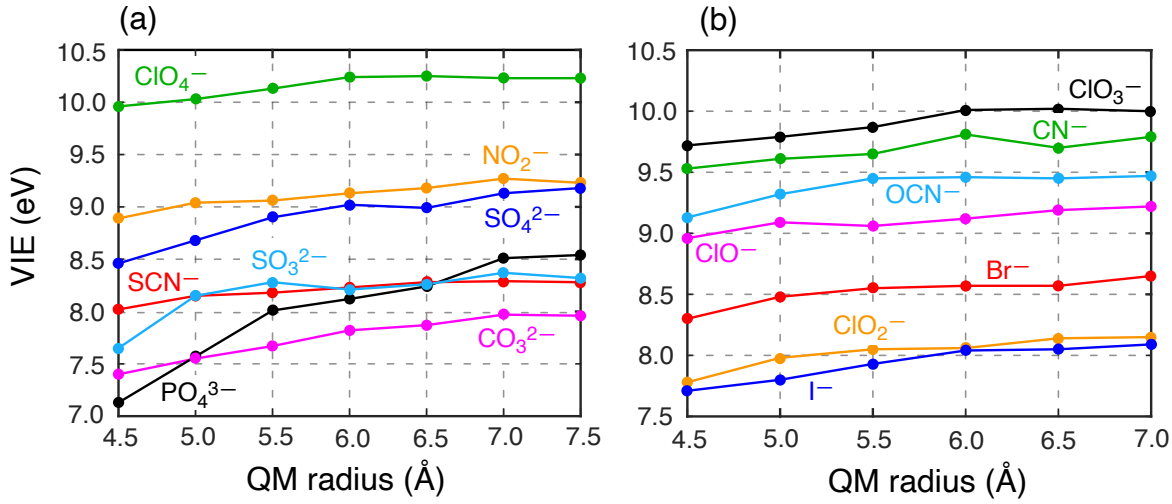

Figure S17: Convergence tests for VIEs as a function of the radius of the atomistic QM region. All calculations use nonequilibrium PCM boundary conditions[57] and the ωB97M-V density functional.

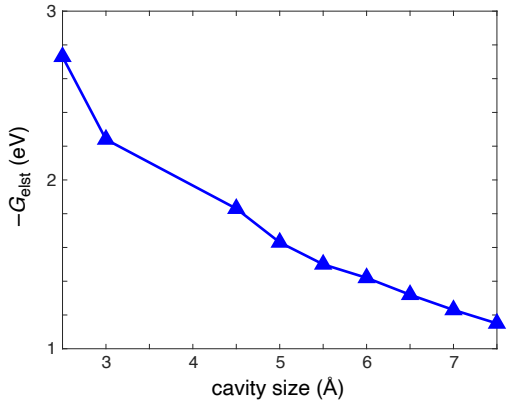

Figure S18: Magnitude of the electrostatic solvation energy, $-G_{\mathrm{elsts}}$, for NO_3^-(aq) as a function of the size of the radius of the cluster of explicit water molecules that is used as the solute in IEF-PCM calculations. As in the Born ion model, the magnitude of G_{elst} varies as $\sim 1/R$ with the radius of the solute. However, the differential solvation contribution to the VIE (ΔG_{elst}) saturates as a function of radius, as shown in Table S8.

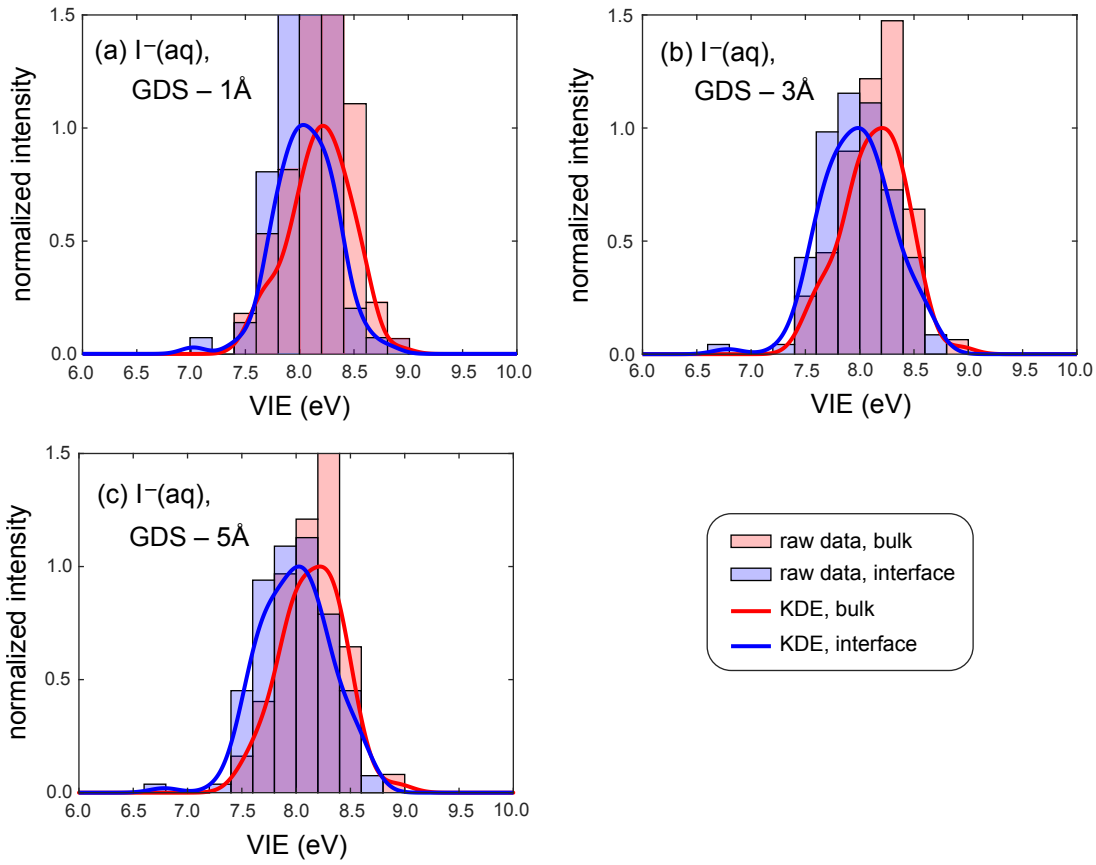

Figure S19: Histograms of the VIE distributions for I^-(aq) in the interior and interfacial regions of a periodic slab simulation, using three different definitions of the bulk/interfacial partition. The curves are the result of kernel density estimation (KDE) applied to the histogram data and are normalized to the same peak height. It is the KDE curves that are plotted in Fig. 3.

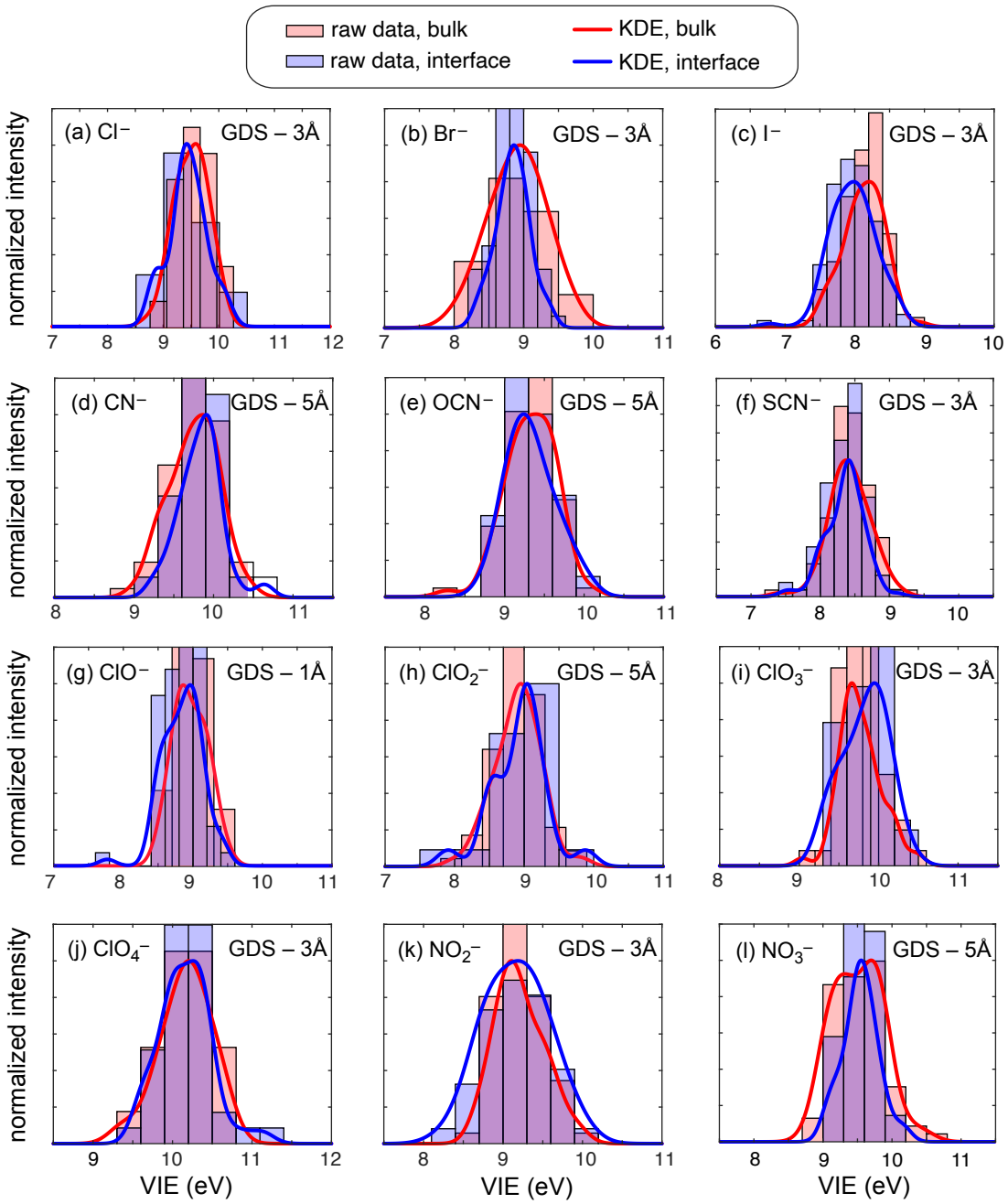

Figure S20: VIE distributions for the monovalent ions from periodic slab simulations, partitioned into bulk and interfacial contributions according to the criterion that is indicated in each panel. What is shown are the histograms of the raw data and the kernel density estimation fits to those histograms.

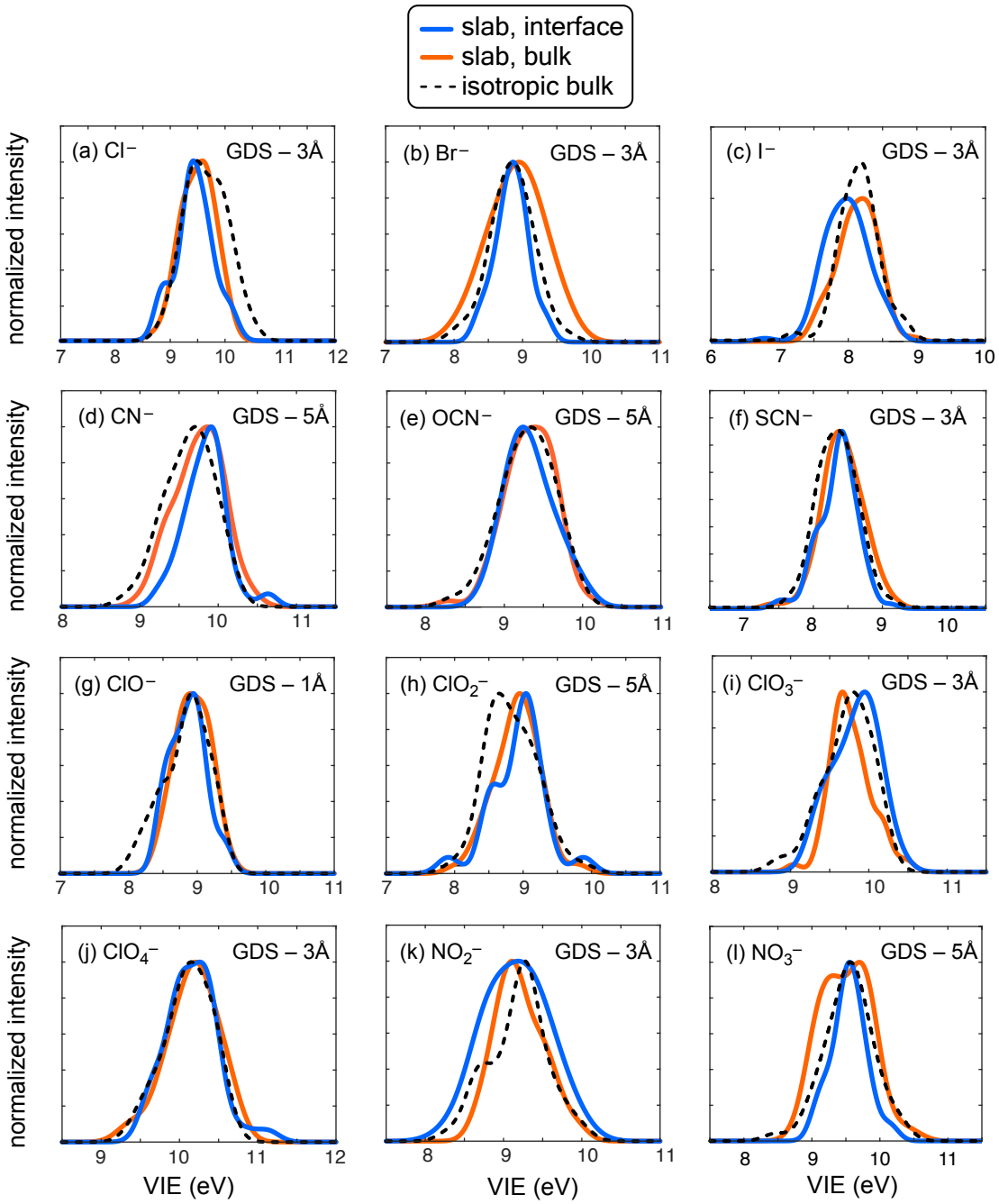

Figure S21: VIE distributions for the monovalent ions from periodic slab simulations, partitioned into bulk and interfacial contributions according to the criterion that is indicated in each panel. Shown are the kernel density estimation fits to histograms of VIEs; see S20 for the histograms themselves. In addition, the isotropic bulk result is shown as well.

Table S1: Comparison of structural parameters for NO_3^-(aq).

Parameter	Expt.[a]	this work	Ref. 15	Ref. 20	Ref. 21
R_{max}(N–O_w)[b] (Å)	3.5±0.3	3.75	3.5	3.4	3.65
R_{max}(N–H_w)[b] (Å)	—	2.6	2.8	2.4	2.75
$\langle CN_1 \rangle$[c]	—	11.0	9.0	10±1	12

[a]Ref. 22. [b]Location of first maximum in the indicated RDF. [c]Coordination number, defined by integrating to the first minimum of the N–O_w RDF.

Table S2: Density profile information for the set of inorganic ions simulated in the $31.34 \times 31.34 \times 156.71$ Å^3 slab. Parameters are obtained from fits of the density profile to Eq. (S1).

Ion	β[a] (Å^{-1})	z_{GDS}[b] (Å)
Br^-	0.56	15.55
I^-	0.62	15.32
CN^-	0.59	15.71
OCN^-	0.61	15.63
SCN^-	0.59	15.62
ClO^-	0.57	15.35
ClO_2^-	0.60	15.64
ClO_3^-	0.59	15.65
ClO_4^-	0.57	15.14
NO_2^-	0.61	15.68
NO_3^-	0.60	15.67
SO_3^{2-}	0.56	15.76
SO_4^{2-}	0.59	15.74
CO_3^{2-}	0.52	15.63
PO_4^{3-}	0.51	15.67

[a]Parameter that defines the length scale of the interface ($\approx 4\beta^{-1}$) in Eq. (S1). [b]Position of the GDS, relative to $z = 0$ at the midpoint of the periodic slab. The value z_{GDS} is the midpoint of the switching region defined by Eq. (S1).

Table S3: Cutoff parameters used to determine the short-range structural metrics. Atom X is the ion's central atom[a] and atom A is the hydrogen-bond acceptor atom.[b] See Fig. S6 for geometric definitions.

Ion	Cutoff (Å)		
	$r(\mathrm{XO_w})^a$		$r(\mathrm{AH_w})^{b,c}$
	CN_1	CN_2	
$\mathrm{Cl^-}$	4.0	6.0	3.0
$\mathrm{Br^-}$	4.4	6.5	3.2
$\mathrm{I^-}$	4.5	6.5	3.4
$\mathrm{CN^-}$	3.6	6.0	2.6
$\mathrm{OCN^-}$	4.6	6.0	2.6
$\mathrm{SCN^-}$	4.9	6.0	2.6
$\mathrm{NO_2^-}$	4.4	6.0	2.4
$\mathrm{NO_3^-}$	4.3	6.0	2.2
$\mathrm{ClO^-}$	5.0	6.0	2.2
$\mathrm{ClO_2^-}$	4.6	6.0	2.4
$\mathrm{ClO_3^-}$	5.0	6.0	2.3
$\mathrm{ClO_4^-}$	5.2	6.0	2.5

[a]X = C for $\mathrm{SCN^-}$, X = N for $\mathrm{CN^-}$, and X = O for $\mathrm{ClO^-}$. [b]A = N for $\mathrm{SCN^-}$ and A = O for the oxyanions. [c]Hydrogen bond cutoff distance, using a cutoff angle $\theta(\mathrm{H_wAO_w}) \leq 30°$ in each case.

Table S4: Spin contamination for the ionized radicals, in the production ωB97M-V calculations.[a] The $\langle \hat{S}^2 \rangle$ values are ensemble averages along each MD trajectory and the uncertainty represents one standard deviation.

Radical	$\langle N_{H_2O} \rangle^b$	$\langle \hat{S}^2 \rangle / \hbar^2$
Cl	30	0.7530 ± 0.0001
Br	45	0.7525 ± 0.0001
I	43	0.7528 ± 0.0001
CN	36	0.7630 ± 0.0007
OCN	36	0.7696 ± 0.0020
SCN	35	0.7609 ± 0.0050
ClO	36	0.7559 ± 0.0005
ClO_2	36	0.7556 ± 0.0030
ClO_3	37	0.7663 ± 0.0030
ClO_4	36	0.7623 ± 0.0020
NO_2	36	0.7574 ± 0.0010
NO_3	36	0.7605 ± 0.0060
SO_3^-	61	0.7595 ± 0.0030
SO_4^-	56	0.7617 ± 0.0010
CO_3^-	58	0.7572 ± 0.0003
PO_4^{2-}	59	0.7606 ± 0.0010

[a]Basis set consists of aug-cc-pVTZ for the ion and 6-31+G* for the water. [b]Average number of explicit water molecules in each electronic structure calculation.

Table S5: Mulliken spin charge (obtained from the spin density $\rho_\alpha - \rho_\beta$) residing on the ionized radical. Values are reported as ensemble averages along each MD trajectory and uncertainties represent one standard deviation.

Radical	$\langle N_{H_2O} \rangle^a$	Mulliken spin charge	
		Hartree-Fock[b]	ωB97M-V[b]
Cl	30	0.97 ± 0.01	0.87 ± 0.11
Br	45	0.98 ± 0.01	0.94 ± 0.01
I	43	0.98 ± 0.01	0.96 ± 0.01
CN	36	0.95 ± 0.02	0.89 ± 0.05
OCN	36	0.99 ± 0.01	0.95 ± 0.02
SCN	35	0.97 ± 0.01	0.94 ± 0.02
ClO	36	0.97 ± 0.01	0.92 ± 0.02
ClO_2	36	0.98 ± 0.01	0.94 ± 0.02
ClO_3	37	0.98 ± 0.01	0.86 ± 0.10
ClO_4	36	0.98 ± 0.01	0.95 ± 0.04
NO_2	36	—[c]	0.93 ± 0.02
NO_3	36	—[c]	0.96 ± 0.02
SO_3^-	61	0.97 ± 0.01	0.90 ± 0.05
SO_4^-	56	0.98 ± 0.01	0.96 ± 0.01
CO_3^-	58	0.98 ± 0.01	0.93 ± 0.01
PO_4^{2-}	59	0.98 ± 0.01	0.93 ± 0.01

[a] Average number of explicit water molecules in each electronic structure calculation. [b] Basis set is aug-cc-pVTZ for the ion and 6-31+G* for the water. [c] Not reported due to wave function stability problems.

Table S6: Gas-phase adiabatic ionization energy (AIE) benchmarks. Experimental uncertainties are all ≤ 0.01 eV except where indicated.

Ion	AIE (eV)	
	experiment	DFT[a]
Cl^-	3.61[b]	3.63
Br^-	3.36[c]	3.36
I^-	3.06[d]	3.17
CN^-	3.86[e]	4.17 (4.17)
OCN^-	3.61[e]	3.50 (3.48)
SCN^-	3.54[e]	3.50 (3.51)
ClO^-	2.28[f]	2.21 (2.20)
ClO_2^-	2.14[f]	2.24 (2.21)
ClO_3^-	4.25[g]	4.30 (4.29)
ClO_4^-	5.25[g]	5.35 (5.39)
NO_2^-	2.27[h]	2.25 (2.23)
NO_3^-	3.94[i]	4.12 (4.18)
MSD[j]	—	0.05 (0.06)
MAD[k]	—	0.09 (0.12)

[a] ωB97M-V/aug-cc-pVTZ(-PP). Values in parenthesis include harmonic zero-point corrections. [b] Ref. 62. [c] Ref. 63. [d] Ref. 64. [e] Ref. 65. [f] Ref. 66. [g] Ref. 67, with reported uncertainty of ± 0.10 eV. [h] Ref. 68. [i] Ref. 69. [j] Mean signed deviation, theory minus experiment. [k] Mean absolute deviation.

Table S7: Comparison of CCSD(T) and ωB97M-V VIEs for hydrated ion clusters, at geometries optimized using ωB97M-V. All calculations use the aug-cc-pVTZ(-PP) basis set for the ion and the 6-31+G* basis set for water. The CCSD(T) calculations correlate valence orbitals only.

Cluster	VIE (eV)		difference
	CCSD(T)	ωB97M-V	(eV)
$Br^-(H_2O)$	3.95	3.98	−0.03
$Br^-(H_2O)_2$	4.53	4.57	−0.04
$Br^-(H_2O)_3$	5.06	5.11	−0.05
$I^-(H_2O)$	3.66	3.67	−0.01
$I^-(H_2O)_2$	4.13	4.15	−0.02
$I^-(H_2O)_3$	4.58	4.61	−0.03
SCN^-	3.50	3.53	−0.03
$SCN^-(H_2O)$	4.04	4.08	−0.04
$SCN^-(H_2O)_2$	4.67	4.72	−0.05
MSD[a]			−0.03

[a] Mean signed deviation

Table S8: Breakdown of the VIEs for NO_3^-(aq), calculated using nonequilibrium IEF-PCM and the ωB97M-V functional, as a function of the radius of the atomistic QM region containing explicit water molecules around the ion. The VIE is decomposed according to VIE = $\Delta U + \Delta G_{\text{elst}}$ [Eq. (S3)], as discussed in the text.

Radius (Å)	VIE (eV)	ΔU (eV)	ΔG_{elst} (eV)
2.5	7.72	4.99	2.73
3.0	8.79	6.55	2.24
4.5	9.10	7.27	1.83
5.0	9.33	7.70	1.63
5.5	9.44	8.44	1.50
6.0	9.46	8.04	1.42
6.5	9.54	8.22	1.32
7.0	9.60	8.37	1.23
7.5	9.64	8.49	1.15

Table S9: VIEs for inorganic ions. Each theoretical value represents an average over 51 snapshots and uncertainties represent one standard deviation, characterizing the width of the distribution. Both the PEqS[29] and PCM[57,59] boundary conditions are used in nonequilibrium mode, where the solvent's optical dielectric constant ($\varepsilon_\infty = 1.8$) is used to adjust the polarization of the continuum upon ionization.

Ion	Expt.[a] VIE (eV)	$\langle N_{H_2O} \rangle$[b]	Vertical Ionization Energy (eV)				
			PCM	Poisson Eqn. Solver (PEqS)			
			ωB97M-V	MP2	ωB97M-V		
			bulk	bulk	bulk		interface
			triple-ζ[c]	double-ζ[d]	double-ζ[d]	triple-ζ[c]	triple-ζ[d]
Cl^-	9.60	30	9.28 ± 0.32	9.49 ± 0.34	9.47 ± 0.29	9.42 ± 0.31	9.45 ± 0.30
Br^-[e]	9.03	45	8.50 ± 0.30	—	8.69 ± 0.29	8.89 ± 0.27	8.84 ± 0.33
I^-[e]	8.34[f]	43	7.90 ± 0.28	—	8.15 ± 0.32	8.07 ± 0.28	8.14 ± 0.31
CN^-	9.60	36	9.53 ± 0.32	10.30 ± 0.37	9.68 ± 0.32	9.64 ± 0.32	9.74 ± 0.30
OCN^-	9.15	36	9.26 ± 0.40	9.87 ± 0.37	9.32 ± 0.34	9.27 ± 0.37	9.32 ± 0.30
SCN^-	8.17	35	8.17 ± 0.27	8.54 ± 0.32	8.35 ± 0.27	8.28 ± 0.27	8.44 ± 0.29
ClO^-	8.59	36	8.69 ± 0.33	9.29 ± 0.38	8.86 ± 0.34	8.83 ± 0.33	8.88 ± 0.32
ClO_2^-	8.22	36	8.57 ± 0.30	9.45 ± 0.32	8.82 ± 0.32	8.84 ± 0.37	8.91 ± 0.32
ClO_3^-	9.66	37	9.64 ± 0.35	10.36 ± 0.36	9.75 ± 0.34	9.63 ± 0.33	9.77 ± 0.26
ClO_4^-	10.07	36	10.05 ± 0.34	10.66 ± 0.39	10.09 ± 0.36	10.11 ± 0.29	10.20 ± 0.32
NO_2^-	8.58	36	9.06 ± 0.37	—	9.20 ± 0.37	9.17 ± 0.30	9.22 ± 0.29
NO_3^-	9.42	36	9.40 ± 0.35	—	9.56 ± 0.36	9.54 ± 0.36	9.56 ± 0.33
SO_3^{2-}	7.84	61	8.01 ± 0.47	8.22 ± 0.41	7.95 ± 0.42	8.12 ± 0.46	8.03 ± 0.54
SO_4^{2-}	9.19	56	8.97 ± 0.32	9.72 ± 0.40	9.18 ± 0.27	9.17 ± 0.30	9.43 ± 0.33
CO_3^{2-}	8.30	58	8.52 ± 0.35	9.35 ± 0.34	8.73 ± 0.36	8.66 ± 0.27	8.72 ± 0.28
PO_4^{3-}	8.54	59	7.88 ± 0.26	8.34 ± 0.33	8.34 ± 0.27	8.33 ± 0.30	8.41 ± 0.29
MAD[g]	—	—	0.23	0.61	0.22	0.21	0.26

[a] From Ref. 51. [b] Average number of water molecules in the atomistic QM region, for the bulk ions. [c] aug-cc-pVTZ basis set for the ion and 6-31+G* for the water. [d] aug-cc-pVDZ basis set for the ion and 6-31+G* for the water. [e] aug-cc-pVXZ-PP (X = D or T) basis sets used for the ion, with corresponding pseudopotentials for the core electrons. Since auxiliary basis sets were not readily available, the RI-MP2 calculations are omitted for these ions. [f] Weighted average of spin-orbit states. [g] Mean absolute deviation between theory and experiment.

Table S10: Bulk VIEs (obtained from isotropic simulations) versus interfacial VIEs (obtained from the interfacial part of a slab simulation), for various anions. The definition of what constitutes the "interfacial part" of the slab simulation is different for different for each ion and can be found in Fig. S20. Also listed are the free energies of solvation (ΔG_{solv}) for the ions.

Ion	VIE (eV)			$\Delta G_{\mathrm{solv}}{}^{a}$
	bulk	interface	difference	(eV)
Cl^-	9.42	9.44	−0.02	−2.3
Br^-	8.89	8.84	0.05	−2.3
I^-	8.07	8.09	−0.02	−2.6
CN^-	9.64	9.83	−0.19	−2.7
OCN^-	9.27	9.33	−0.06	−2.7
SCN^-	8.28	8.46	−0.18	−2.3
ClO^-	8.83	8.86	−0.03	−3.1
ClO_2^-	8.84	8.92	−0.08	−3.0
ClO_3^-	9.63	9.83	−0.20	−2.8
ClO_4^-	10.11	10.16	−0.05	−2.6
NO_2^-	9.17	9.16	0.01	−2.9
NO_3^-	9.54	9.54	0.00	−2.6
SO_3^{2-}	8.12	8.24	−0.12	−10.4
SO_4^{2-}	9.17	9.45	−0.28	−10.2
CO_3^{2-}	8.66	8.65	0.01	−11.1
PO_4^{3-}	8.33	8.36	−0.03	−22.3

[a] ωB97M-V/aug-cc-pVTZ + SMD solvation model.[70]